UNIVERSITY OF
LATVIA

Summary of
Doctoral Thesis

Austris Akmentinsh

MODELLING SHALLOW CONFINEMENT IN TUNEABLE QUANTUM DOTS

Riga 2025

UNIVERSITY OF
LATVIA

FACULTY OF SCIENCE
AND TECHNOLOGY

Austris Akmentinsh

MODELLING SHALLOW CONFINEMENT IN TUNEABLE QUANTUM DOTS

SUMMARY OF DOCTORAL THESIS

Submitted for the degree: Doctor of Philosophy

Field: Physics, Astronomy and Mechanics

Subfield: Solid state physics

Riga 2025

This doctoral thesis was done at the University of Latvia, Faculty of Physics, Mathematics and Optometry (since September 2024, part of the Faculty of Science and Technology), in the Department of Physics, at the Chair of Theoretical Physics, during the period from 2019 to 2024.

The doctoral thesis consists of 6 chapters, including introduction and conclusions. Additionally, there is a bibliography, but no appendices. A summary of the thesis is available in both English and Latvian, with the English version being the primary one. The Latvian version was obtained by first translating the English version using the artificial intelligence tool *ChatGPT*, followed by subsequent careful editing.

Thesis format: dissertation in the field of Physics and Astronomy, subfield of Solid State Physics.

Scientific supervisor: Professor, *Dr. phys.* **Vjačeslavs Kaščejevs**, University of Latvia, Latvia.

Referees:

1. Dr. Akira Fujiwara, NTT Basic Research Laboratories, Japan,
2. Dr. Frank Hohls, German National Metrology Institute (PTB), Germany,
3. Dr. rer. nat. Sergejs Piskunovs, Institute of Solid State Physics, Latvia

The defense of the thesis will take place at an open meeting of the Promotion Council of Physics and Astronomy of the University of Latvia on the 13th June,

Time and location of the meeting

The dissertation and its summary are available at the Library of University of Latvia, Riga, Kalpaka bulvāris 4.

Chair and Secretary of the Promotion Council of Physics and Astronomy of University of Latvia:

Chair, Uldis Rogulis

Secretary, Sintija Siliņa

ISBN 978-9934-36-390-0
ISBN 978-9934-36-391-7 (PDF)

ABSTRACT

One physical system which realizes the generic scenario of an electron tunneling through a barrier out from a potential well is a tuneable barrier quantum dot. Pushing many of its applications to the limits of its fastest possible operation requires the tunneling to be as large as possible which inevitably pushes the dot to the brink of losing its confining properties. The focus of this doctoral thesis is this shallow regime of confinement where the dot can hold a single electron in a single or a couple of discrete states. By considering the one-dimensional cubic potential we hope to describe universal properties of such weakly confined electrons that would characterize them over a wide range of experimental realizations.

We use the cubic assumption to model single electron capture in dynamically modulated quantum dot experiments under a variety of physical conditions: 1) adiabatic evolution of the electron through the local ground states of the dot 2) under the additional influence of temperature 3) or under the additional influence of magnetic field. By comparing our model predictions with data counting single electron capture events or measuring the pump current we are able to verify the cubic potential hypothesis over multiple quantum dot realizations and driving protocols. Moreover, we are able to characterize experimental dots in a variety of ways: we are able to characterize the number of available confined states, we determine a dimensionless driving speed which estimates how close the microscopic dynamics is to non-adiabatic excitation, we estimate the barrier height of the dot, its tunnel rate and more. Finally, we are also able to estimate a frequency which, we predict, limits the operation speed of quantum-dot-based devices and which could be optimized to make them faster.

Keywords: tuneable barrier quantum dot, shallow confinement, cubic potential.

Contents

1. MOTIVATION AND BROADER OVERVIEW

In this introductory chapter, we give the necessary context to motivate and understand the research presented in this thesis. In this work, the physical system at the center of attention will be the tuneable barrier quantum dot. Thus, sec. 1.1 first locates general research on them within the broad field of physics. Further, sec. 1.2 properly defines them and explains in some detail how they can be made and sec. 1.3 describes two of their applications. This is then used in sec. 1.4 to broadly motivate and describe the original research presented in this particular work.

1.1. Introduction

The research presented in this doctoral thesis is part of the broader scientific field called nanoscience and nanotechnology. The emergence of such a field was predicted already in 1959 by the legendary physicist R. P. Feynman in his visionary talk "There's Plenty of Room at the Bottom" [1]. In it he discusses the possibility of synthesizing new molecules by moving individual atoms one-by-one, draws inspiration from biology to build "tiny machines", predicts the miniaturization of computers and information storage and more. Even though serious work in nanoscience began only later it has since been very successful and has acquired a wide scope of questions investigated. The existing research directions include: nanomaterials, molecular machines, nano-scale sensors and devices, photonic structures, quantum information, nanobiotechnology and more. The research of this thesis would mostly be categorized under nano-scale electronic devices.

In general, a **quantum dot (QD)** is a small region in a solid state system, with a size on the order of nanometers, that confines electrons and has discrete energy levels similarly to an atom. A variety of systems with these properties is possible and one noteworthy example are the nanoparticle QDs for which the 2023 Nobel prize in chemistry was awarded [2]. However, the QDs considered in this work – tuneable barrier quantum dots [3] –, rather than being static regions of the solid with fixed properties in time, can have dynamically changing properties chosen externally by the experimenter.

1.2. Tuneable barrier quantum dots

In this section, we introduce the physical system which is at the center of this doctoral thesis – the tuneable barrier quantum dot. We describe the different physical mechanisms used for confining electrons in it, define its main characteristic quantities and briefly mention the related many-body aspects. For more comprehensive reviews see [3, 4].

Tuneable barrier quantum dots are artificially fabricated semiconductor devices which can be used for precise manipulation of single electrons. In fig. 1.1a we give an example in gallium arsenide. To create such a device one, first, uses a layered structure consisting of two different materials so that at the interface the lowest energies of the conduction band, everywhere else above the Fermi energy ϵ_F, sink somewhat below ϵ_F. Because of this, the electrons in the 2D interface become mobile, thus, collectively creating the so-called **two-dimensional electron gas** (2DEG) [5]. Further confinement – from two-dimensional to one-dimensional – can be achieved by modifying the shape of the electron carrying interface in a chemical process called etching [6]. A **tuneable** QD can finally be formed as an electrostatic potential energy well by using **gates** – metallic electrodes to which experimentally tuneable voltages can be applied. In fig. 1.1a there are two such gates and they are marked with their respective voltages – the **source gate voltage** $\mathbf{V_S}$ and the **drain gate voltage** $\mathbf{V_D}$ for isolating the QD from the source and drain electron reservoirs, respectively.

Having created a QD we can have a closer look at its main properties which we illustrate in fig. 1.1b. The main feature of the QD is the existence of a discrete set of quantum states available to an electron trapped inside. Each of these states is characterized by: 1) a discrete energy ϵ_n and 2) a pair of tunnel rates $\Gamma_{n,S}$ and $\Gamma_{n,D}$ for escaping through either the source or drain barrier. To model the dependence of these quantities on gate voltages two simple relations can be assumed – linear [7] for the energies ϵ_n and exponential [8] for the tunnel rates Γ_n. For example,

$$\Delta\epsilon_n = -\alpha_S^{(\epsilon)}\Delta V_S - \alpha_D^{(\epsilon)}\Delta V_D, \qquad \alpha_i^{(\epsilon)} > 0 \tag{1.1a}$$

$$\Gamma_{n,S} = \Gamma_{n,S}(0,0)\, e^{-\alpha_S^{(\Gamma)}V_S - \alpha_D^{(\Gamma)}V_D} \qquad \alpha_S^{(\Gamma)} < 0,\ \alpha_D^{(\Gamma)} > 0 \tag{1.1b}$$

Regarding the many-body aspect, in general, different numbers of confined electrons in the QD are possible. In thermal equilibrium, this is largely determined by the Fermi energy ϵ_F and temperature T of the whole system. For negligible Coulomb interactions between electrons in the QD all the single-particle discrete states of the QD will have an occupation probability following the Fermi-Dirac statistics $f(\epsilon) = (1+e^{(\epsilon_n-\epsilon_F)/k_BT})^{-1}$. In the opposite case of strong Coulomb interactions the thermal equilibrium number of captured electrons can be very well defined and, also, the decay rates Γ of states with different captured electron numbers may have different typical scales.

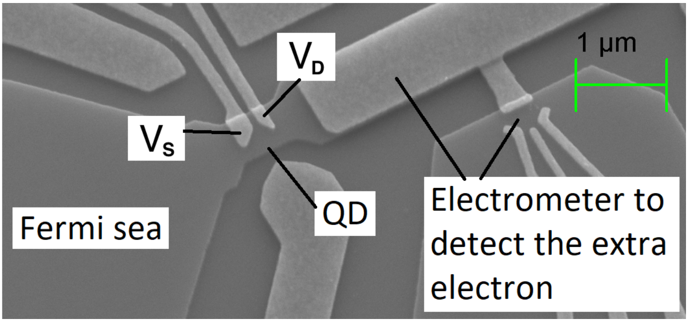

(a) Experimental tuneable barrier quantum dot (QD)

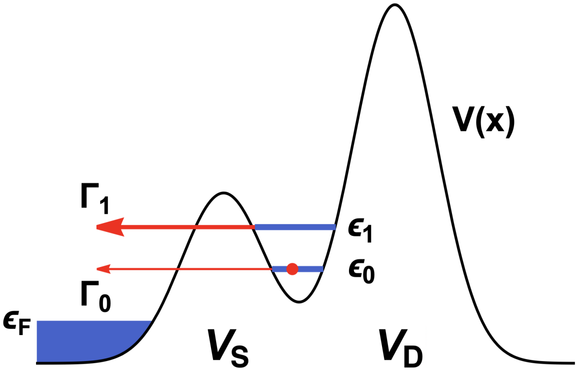

(b) One-dimensional model of a tuneable barrier quantum dot

Figure 1.1: **(a)** An experimental GaAs/AlGaAs tuneable barrier quantum dot. The mobile electrons manipulated by such a device form a two-dimensional layer at the GaAs/AlGaAs interface. For this particular device, this interface is in the shaded region whose lower-left part is marked as "Fermi sea", which continues up-right where it is marked as "QD" (quantum dot) and even further up-right where it is covered by a part of the electrometer. Using experimentally tuneable voltages V_S and V_D, applied to metallic gate electrodes (shaded light-grey), a QD can be formed for the mobile electrons as an electrostatic potential energy well. **(b)** A tuneable barrier QD modelled using a one-dimensional potential energy $V(x)$. The two gate voltages V_S and V_D each create a corresponding potential barrier in $V(x)$ and the potential well in-betwenn corresponds to the QD. Inside the well, a confined electron has a number of discrete states available to it, each characterized by an energy ϵ_n and a tunnel rate Γ_n into the source lead. In the source lead, there is a Fermi sea of electrons with Fermi energy ϵ_F.

1.3. Applications of tuneable barrier quantum dots

In this section, we review two applications of tuneable barrier QDs. The more established application is their use in metrology as single electron pumps to generate highly precise reference currents at scales $\lesssim 10^{-10}$ A while a more recent application is their use as single electron sources in a novel field of research in solid state physics called electron quantum optics. Tuneable barrier QDs can also be used for quantum computing with spin qubits [9, 10, 11], however, we do not elaborate more on this here.

The main idea of single electron pumping is to take a tuneable barrier QD, connect it to two electron reservoirs and operate it periodically with frequency f such that during a single period, at one stage, n electrons are captured in the QD from the source reservoir and then, at a later stage, these same n electrons are released into the drain reservoir. If the number n of electrons can be held stable then a current with a very precise value

$$I = nef \tag{1.2}$$

flows through the QD between the source and the drain. As a process which can generate highly precise currents this is very valuable in the field of science and technology called metrology whose task is to ensure that all measurements on a global scale – from the ones at the cutting edge of science to very mundane ones – are all consistent with each other and as precise as possible.

The currently most successful mechanism for operating tuneable barrier QDs to achieve high current precision is called single-parameter nonadiabatic pumping [13, 14, 15]. Here, one leaves the source-drain voltage unbiased and modulates in time only the source gate voltage V_S while the drain gate voltage V_D is kept fixed in time. Additional factors improving the precision of the generated current, especially for GaAs devices, have been found to be the application of a magnetic field [16, 17, 18] and the usage of specially shaped (red curve in the inset of fig. 1.2) voltage pulses $V_S(t)$ [19]. With this, there have been several experimental demonstrations [4, 12, 19, 20, 21] for an $I = ef$ current with metrologically relevant relative uncertainties $10^{-7} - 10^{-6}$. Fig. 1.2 shows the particular work in [12] – the main graph in fig. 1.2 shows the measured current I depending on the drain gate voltage V_D. Pronounced current plateaus can be observed at the quantized values nef of eq. 1.2 which is strong evidence that, indeed, a stable number n of electrons gets transported through the QD per cycle.

Of course, there is still room for improving the electron pump technology. For example, to know the value of the experimental output current with higher precision work has been done [22, 23] to directly detect and measure the distribution of specific electron transport errors $n \pm 1$, $n \pm 2 \ldots$

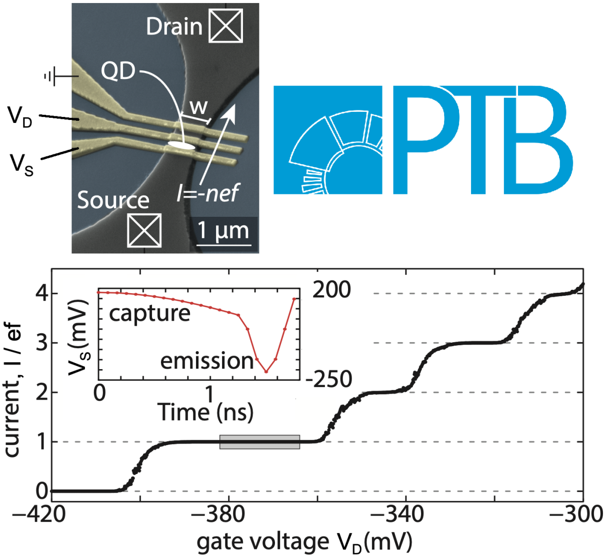

Figure 1.2: Adapted from [12]. Demonstration of a pump current $I = ef$ with relative uncertainty $2 \cdot 10^{-7}$. Upper image: SEM micrograph of the electron pump. Electrons flow through the region shaded in black. The QD is located between the two gate electrodes marked by their gate voltages V_S and V_D. Main graph: the current generated by the electron pump as a function of the time-independent drain gate voltage V_D. Pronounced plateaus of the current at the quantized values of $I = nef$ are observed.

during a pump cycle. Right now, this is still possible at low frequencies f and currents I. Another direction for improvement would be increasing the maximum high-precision output current so that the single electron pump realization of the Ampere would be more widely applicable. The first approach to do this would be to simply increase the pump frequency f in $I = nef$. However, it is known [24] that at frequencies $f \lesssim 1\text{GHz}$ corresponding to $I \lesssim 100$ pA the current plateaus of $I(V_D)$ degrade and the relative uncertainty of the quantized current increases. For this phenomenon, the results of this doctoral thesis will be relevant as our work will mainly be motivated by the fast operation limit of such devices.

A more recent application of tuneable barrier QDs is their use as on-demand single electron sources in electron quantum optics experiments. Here, one essentially takes a single electron pump, operates it as above, but this time follows the ejected electron in the circuit to see what happens to it and how it can be used or manipulated further. Due to the ejected electrons traveling downstream as waves the experiments performed with them resemble quantum optics to a great extent and, hence, the name electron quantum optics. Nevertheless, due to the differences between electrons and photons, like different exchange statistics and presence / absence of Coulomb interactions, the electronic version would be like an exotic regime of quantum optics.

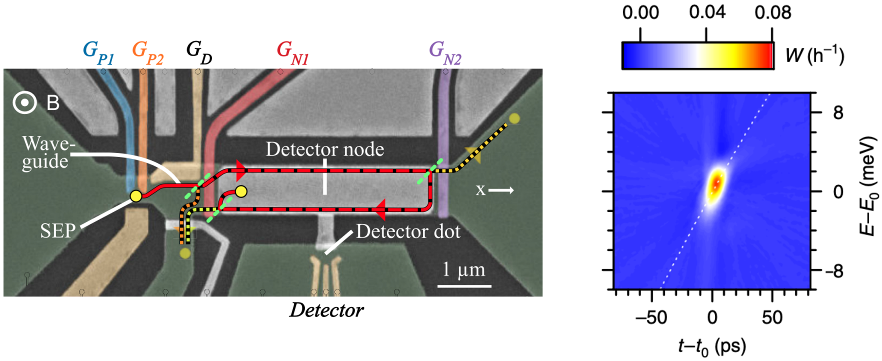

(a) Electron quantum optics experiment **(b)** Inferred $W(t, E)$

Figure 1.3: (a) Adapted from [25]. A GaAs/AlGaAs chip for doing electron quantum optics experiments. The single electron source is marked by the left-most yellow dot. Electronic wave-guides are marked by the solid or dashed red lines and also the dotted lines. The beam-splitters are shown as the green dashed diagonal lines. The single electron detector uses the detector dot to measure changes of electric charge in the detector node. **(b)** Adapted from [26]. Tomographically reconstructed quantum state of an electron emitted from a QD-based single electron source. The quantum state is represented here by the corresponding Wigner quasiprobability distribution $W(t, E)$ in time-energy coordinates.

In fig. 1.3a, adapted from [25], a semiconductor chip is shown which contains electronic analogs for all the necessary quantum optics elements: 1) the single electron source is simply the single electron pump, 2) the wave-guide is realized as a quantum Hall edge channel for which a sufficiently strong magnetic field is necessary, 3) beam-splitters are realized by tuneable partially transmitting potential barriers and 4) single electrons in specific regions of interest can be detected by detecting changes in charge there. To have reasonable expectations for the possible effects in experiments with such systems one should know what is the quantum state initially supplied by the tuneable barrier QD. For this, a full tomographic protocol is possible [27] and fig. 1.3b, taken from [26], shows one such supplied state as a Wigner quasi-probability distribution $W(t, E)$ in energy-time axes. Although this will not be done in this doctoral thesis the model introduced in it could be used for modeling $W(t, E)$ in the regime of rapid electron emission.

1.4. Motivation, scope and structure of the thesis

The main focus of this doctoral thesis – the study of the one-dimensional cubic potential for describing tuneable barrier quantum dots – is motivated from the fast operation limit of tuneable barrier QDs. The regime of fast operation can be practically significant for both kinds of the previously presented applications of QDs – the single electron pump as well as the on-demand electron source. For single electron pumps, the fast operation regime means a large pump frequency f and, correspondingly, a large targeted quantized output current $I = nef$. However, currently, increasing the pump frequency above $f \sim 1\,\mathrm{GHz}$ degrades the precision [24] of the output current value $I = ef$ and understanding why this happens and if it can be avoided would be beneficial for the metrological application of single electron pumps at an increased $\sim 1\,\mathrm{nA}$ current level. For the on-demand electron source application, the fast operation regime means ejecting an electron fast and with a small temporal width in the electron quantum optics device. Such a small temporal width would imply high temporal resolution of an electron quantum optics interferometer used for sensing and in quantum computing applications this could enable fast information processing.

The regime of fast operation of QD-based devices largely coincides with the regime of a shallow QD with only weak confinement of electrons because for the necessary tunneling processes to happen fast enough the corresponding tunnel rates have to be sufficiently large. The tunneling processes under question could be, for example, the emission of an on-demand electron from an electron source or, in the case of single electron pumps during the capture phase, the emission of an extra second electron in the QD back to the source to remain with the target number of a single captured electron, $n = 1$.

In this doctoral thesis, our aim is to explore the shallow regime of confinement using a simple theoretical model. For simplicity we take a one-dimensional model and to describe the essential properties of shallow confinement we choose a cubic polynomial for the potential energy confining the electron. As a cubic polynomial should be an adequate approximation locally to many time-dependent one-dimensional potential energies close to the transition between having and not having a local minimum we hope to describe with this model universal properties of weakly confined electrons in a wide range of real experimental systems provided they are operated in a shallow or fast enough regime. We use the cubic potential assumption to consider the case of a single captured electron with only a single or a couple of confined states available to it and model the capture phase of a single electron pump cycle at various physical conditions. For all the considered scenarios, the corresponding capture probabilities of the model are compared to experimental data to either confirm the experimental realization of the model or to characterize the experimental QDs using model quantities of the cubic potential. As a result, the following theses, which can be defended by the findings in this work, can be formulated:

Defendable theses:

1. The one-dimensional cubic potential is a relevant model for electron confinement in shallow quantum dots.
2. All cubic model parameters of a real system can be deduced from charge capture experiments.
3. A single time-energy scale determines the physical limits on speed and accuracy of single-electron capture by tuneable-barrier quantum dots.

We give now a brief overview of the content of each individual chapter: in chapter 2 we introduce the one-dimensional cubic potential and its characteristic quantities. We identify a frequency scale of the model which can be interpreted as the speed of a device. In chapter 3 we model the baseline scenario where the electron state in the QD remains adiabatically the local ground state. Here, we introduce a data-analysis technique, which we will use throughout this thesis, for combining different electron capture probabilities obtained using different QD closing speeds into a single master curve. In chapter 4 we model temperature effects in the cubic potential using transition state theory. From this, we show how to estimate the above speed of a device and, further, characterize the device using any quantity of the cubic model. We continue in chapter 5 where we show how the one-dimensional cubic model can be used even in the presence of a non-zero magnetic field provided that either magnetic or transverse electrostatic confinement is stronger than the electrostatic longitudinal cubic confinement. Finally, we conclude in chapter 6 where we state our main findings.

2. CUBIC POTENTIAL MODEL

In this chapter, we introduce the cubic potential model – the mathematical basis for modeling shallow QDs on which all of the following work in this thesis will stand. In sec. 2.1 we motivate this model and introduce its main quantities for the case of a static cubic potential. In sec. 2.2 we present the time-dependence of the potential that we will use to describe electron capture experiments. We find a frequency scale which, we think, will be important in future for optimizing QD-based devices towards faster operation. Finally, in sec. 2.3 we show the relation of the cubic model to Josephson junctions which we will use later in chapter 4.

2.1. Motivation and the main quantities and scales

The one-dimensional cubic polynomial as a potential energy for a confined particle can be motivated as the simplest possible model for metastability because these are the lowest possible order polynomials where a finite well next to an open infinite region is possible. We expect such a model to be physically relevant in scenarios where a one-dimensional time-dependent potential energy $V(t, x)$ can be used to describe a system which is transitioning between two regimes – not having and having confinement. Then, as illustrated in fig. 2.2 with two consecutive snapshots of $V(t, x)$, a cubic polynomial approximation for the potential would be appropriate. Due to the generality of this approximation (biggest assumption – one-dimensionality, for an analysis of this see in the main work the corresponding section to this one) we hope to describe with it universal behavior of a wide range of real experimental systems.

Regarding the parametrization of the cubic potential we only view two of its parameters as physically significant because the second and zeroth powers can be made to vanish by the right choice of spatial origin and energy reference level. Then, the remaining third power will determine an important frequency scale for a confined particle and the first power will be crucial for switching the potential from non-confining to confining. From this, the potential energy that we will use throughout this thesis will be

$$V(x) := b\,x^3/3 - F\,x + V_b/2 \tag{2.1}$$

where the constant term $V_b/2$ ensures that the energy reference level, $V = 0$, is located at the local minimum $x = x_0$ of the potential. The two independent physical scales, the barrier height $V_b = (4/3)\sqrt{F^3/b}$ and the spatial scale of the well, $x_0 = \sqrt{F/b}$, are illustrated in fig. 2.2a.

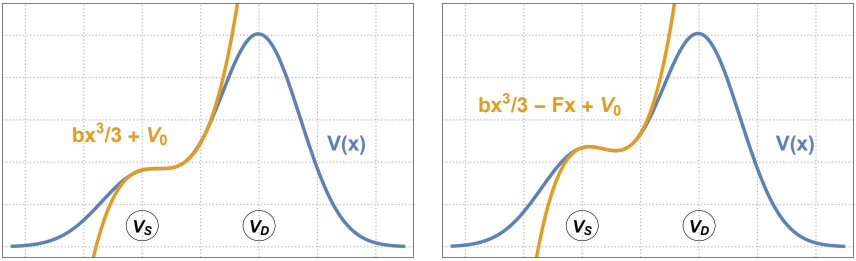

(a) Birth of a QD **(b)** A shallow QD

Figure 2.1: Main idea for using the cubic potential. (a) $V(x)$ – a one-dimensional electrostatic potential on the verge of having a potential well – a QD. In the region where the QD is about to form the potential is well described by the cubic function $V(x) \approx bx^3/3 + V_0$. (b) $V(x)$ – a one-dimensional electrostatic potential where a QD has formed. If the corresponding potential well is not too deep then it can still be described by a cubic function, $V(x) \approx bx^3/3 - Fx + V_0$.

Adding the kinetic energy to $V(x)$ we obtain our model Hamiltonian

$$\mathcal{H} = -\frac{\hbar^2}{2m}\frac{d^2}{dx^2} + b\,x^3/3 - F\,x + V_b/2 \tag{2.2}$$

This defines the small oscillation frequency $\omega_0 = (2/m)^{1/2}\,(bF)^{1/4}$ around the local minimum x_0 together with the corresponding harmonic oscillator energy scale $\hbar\omega_0$, both illustrated in fig. 2.2a. Taking the ratio between the barrier height V_b and the harmonic level spacing $\hbar\omega_0$

$$u := \frac{V_b}{\hbar\omega_0} = \frac{2\sqrt{2m}}{3\hbar}\frac{F^{5/4}}{b^{3/4}} \tag{2.3}$$

gives a dimensionless depth u of the cubic QD as well as an approximate number of its discrete confined quantum states as illustrated in fig. 2.2b. We will use this dimensionless quantity extensively to characterize the strength of confinement of a particle inside the cubic potential well.

The harmonic oscillator of $\mathcal{H}$ at the potential minimum can be made more visible by using the coordinate $\mathrm{x} := (x - x_0)\sqrt{m\omega_0/\hbar}$. Then,

$$\mathcal{H} = \hbar\omega_0\left(-\frac{1}{2}\frac{d^2}{d\mathrm{x}^2} + \frac{\mathrm{x}^2}{2} + \frac{\mathrm{x}^3}{3\sqrt{6u}}\right) \tag{2.4}$$

As can be seen, increasing the depth u suppresses the anharmonicity given by the cubic term $\propto \mathrm{x}^3$. Thus, u can also be seen as a harmonicity parameter in this problem.

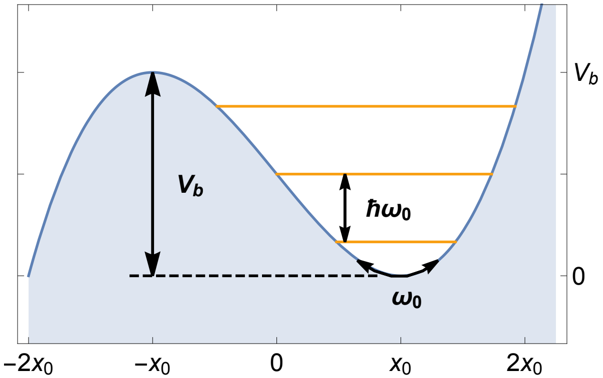

(a) Characteristic scales

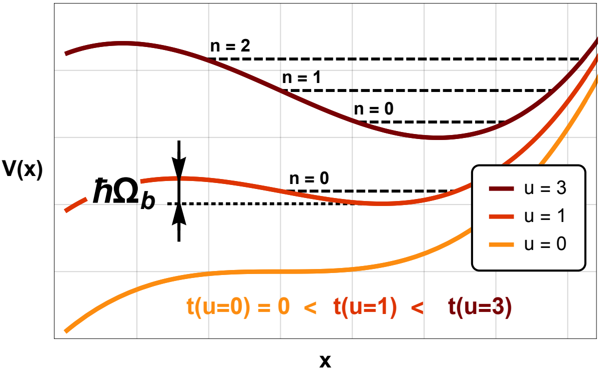

(b) Model dynamics

Figure 2.2: **(a)** The cubic potential $V(x)$, eq. (2.1), its meta-stable confined discrete states in the harmonic approximation and the corresponding physical scales: V_b – the barrier height of the confinement potential, x_0 – location of the potential minimum, also half of the distance between the local maximum and minimum, ω_0 – small oscillation angular frequency around the local minimum, $\hbar\omega_0$ – level spacing between the confined meta-stable energy states in the harmonic approximation. **(b)** Time-dependence of the cubic potential $V(t,x)$ in $\mathcal{H}(t)$, eq. (2.5), during a capture experiment of an electron. The cubic QD appears at $t = 0$ and then gradually gets deeper with an increasing number of confined states $u(t) = (t/t_c)^{5/4}$. Due to the assumed time-independence of b the process is characterized by an energy scale $\hbar\Omega_b = \hbar(6\hbar b^2/m^3)^{1/5}$ and the corresponding time-scale Ω_b^{-1} for the internal electron dynamics.

2.2. Time-dependence

To be able to describe electron capture experiments we need to introduce time-dependence $\mathcal{H}(t)$ in our model Hamiltonian, eq. (2.2). To describe the immediate effects of the transition between non-confining and confining situations and to keep the model as simple as possible we leave the third power coefficient b time-independent and consider linear dependence for the linear coefficient, $F(t) = \dot{F}\, t$. Thus,

$$\mathcal{H}(t) = -\frac{\hbar^2}{2m}\frac{d^2}{dx^2} + b\,x^3/3 - \dot{F}\,t\,x + V_b(t)/2, \qquad \dot{F} > 0 \tag{2.5}$$

To qualitatively analyze the corresponding dynamics we choose 3 physical scales of the time-dependent problem. For energy, we take the barrier height V_b and level spacing $\hbar\omega_0$ at $u = 1$ when they are equal. Here, we define the energy scale as $\hbar\Omega_b := \hbar\omega_0 = V_b$ where

$$\Omega_b := \omega_0(u = 1) = \left(\frac{6\hbar b^2}{m^3}\right)^{1/5} \tag{2.6}$$

From this, we can choose for the spatial scale of $\mathcal{H}(t)$ the corresponding harmonic oscillator confinement scale $\sqrt{\hbar/m\Omega_b}$. Finally, for the characteristic time scale we choose $t_c := t|_{u=1} - t|_{u=0}$, the time interval between $u = 0$ and $u = 1$. Using variables $t_{DL} = t/t_c$ and $x_{DL} = x\sqrt{m\Omega_b/\hbar}$ we can write a dimensionless Schrodinger equation

$$i\frac{\partial\psi}{\partial t_{DL}} = \frac{5}{4}\frac{\omega_0}{\dot{u}}\left(-\frac{1}{2}\frac{d^2}{dx_{DL}^2} + \frac{x_{DL}^3}{3\sqrt{6}} - \frac{\sqrt{3}\,t_{DL}}{2\sqrt{2}}x_{DL} + \frac{t_{DL}^{3/2}}{2}\right)\psi \tag{2.7}$$

which depends on a single parameter, a dimensionless speed for closing the QD

$$\frac{\dot{u}}{\omega_0} = \frac{5}{6}\frac{m}{\hbar}\frac{\dot{F}}{b} \tag{2.8}$$

Qualitatively, the ratio $\dot{u}/\omega_0$ compares two microscopic speeds: 1) the rate $\dot{u}$ at which new confined levels appear in the cubic well – how fast does the potential change – and 2) the small oscillation angular frequency ω_0 – how fast does the state of the electron change. The main attention of this thesis will be given to the regime $\dot{u}/\omega_0 \ll 1$ where we expect adiabatic evolution of the electron state without transitions between the discrete states n. Thus, escape from the QD will only happen by tunneling with continuously decreasing tunnel rates $\Gamma_n(t)$ and the final escape probability will be determined by a competition between $\Gamma_n(t)$ and the time scale $t_c \sim \dot{u}^{-1}$ on which the cubic barrier becomes non-transparent. At increased speeds, $\dot{u}/\omega_0 \sim 1$, we expect non-adiabatic transitions to complicate this simple tunneling picture.

Thus, the qualitative behaviour of the escaping / captured electron will be determined by a single dimensionless speed parameter $\dot{u}/\omega_0$. On the other hand, the physical time scale on which a system will actually realize this behavior will be proportional to the inverse frequency Ω_b^{-1} because

$$t_c := t|_{u=1} - t|_{u=0} = \frac{5}{4}\frac{\Omega_b^{-1}}{\dot{u}/\omega_0} \tag{2.9}$$

Here, the speed parameter $\dot{u}/\omega_0$ accounts for different possible speeds of closing the dot and in an experiment this would be tuneable. The overall scale of t_c, however, is given by Ω_b^{-1} which would not be tuneable and which would be a parameter of the device. Thus, we see that for experimental devices the frequency scale Ω_b could be interpreted as a speed of the device – the larger Ω_b the faster the device would realize the same cubic model Schrodinger equation (2.7) and one of its solutions. E. g., for the metrological electron pumps of sec. 1.3 this would mean realizing the capture process of an electron faster, but, for example, without non-adiabatic excitations as long as the dimensionless speed parameter $\dot{u}/\omega_0$ would be kept small enough. Similarly, for the single electron sources of sec. 1.3 (for which $\dot{F} < 0$ in eq. (2.5)) a larger Ω_b would imply a faster emission of the electron from the dot.

2.3. Relation to Josephson junctions

We now briefly explain how the one-dimensional cubic model can also be relevant in Josephson junctions from superconducting physics. The generalized coordinate used for describing Josephson junctions is the flux $\phi(t) := \int_{-\infty}^{t} V(t')dt'$ where $V(t)$ is the voltage across the junction. The corresponding canonically conjugate variable is the charge q accumulated at the junction in one of the superconductors [28]. Generally, a Josephson junction is characterized by 2 parameters – the capacity C which characterizes the junction as a simple plate capacitor and the critical current I_0 which is the maximal superconducting current possible in the junction.

Connecting the junction to other circuit elements can make its ability to carry a superconducting current vanish. Around this transition, the junction can be described by the Hamiltonian [29]

$$\mathcal{H}_{\rm JJ} = -\frac{\hbar^2}{2C}\frac{d^2}{d\phi^2} - \left[\frac{I_0}{2}\left(\frac{2\pi}{\phi_0}\right)^2\frac{(\delta\phi)^3}{3} - (I_0 - I)\delta\phi\right] \tag{2.10}$$

where the experimentally tuneable bias current I characterizes the external circuit elements, $\phi_0 := \pi\hbar/e$ and $\delta\phi := \phi - \phi_0/4$. We see that this is, essentially, the cubic potential Hamiltonian, eq. (2.2), written for the varible ϕ. We can identify the 3 parameters of eq. (2.2) here as

$$m \to C \qquad F \to I_0 - I \qquad b \to \frac{I_0}{2}\left(\frac{2\pi}{\phi_0}\right)^2 \tag{2.11}$$

These relations can be used as replacement rules in various expressions which hold true in the cubic model to characterize a Josephson junction in the corresponding regime. Like this, we will compute and use the cubic model quantities ω_0, V_b, u and Ω_b for the experimental junctions in [30, 31].

3. ADIABATIC TUNNELING FROM THE GROUND STATE

In this chapter, we model single electron capture in the QD in our baseline scenario – the electron remaining adiabatically the whole time in the local ground state of the QD. In sec. 3.1, using a simple kinetic equation model, we obtain a scaling relation for the electron capture probability with respect to different closing speeds of the QD. This scaling relation predicts the appearance of a single master curve in electron capture probability data with several different closing speeds. This prediction is verified in two experimental datasets in sec. 3.2 where we obtain two such master curves. To predict their precise shape using the cubic model, in sec. 3.3 we compute precise tunnel rates out of the cubic potential well. With this, we compare in sec. 3.4 the experimental and the cubic model master curves and find excellent agreement, which allows us further characterizing the experimental QDs in terms of dimensionless cubic model quantities.

3.1. Kinetic equation and the scaling relation

Our mathematical basis for modelling the capture probability of an electron in a QD will be the simple kinetic equation

$$\frac{dP}{dt} = -\Gamma(t)\Big(P(t) - f(\epsilon_0(t))\Big), \qquad \Gamma > 0 \tag{3.1}$$

which rests on the theoretical notions of a QD introduced in sec. 1.2 and fig. 1.1b. Here, $P(t)$ is the probability that the QD is populated by an electron, Γ describes tunneling in and out of the QD and $f(\epsilon_0) = (1 + e^{(\epsilon_0 - \epsilon_F)/k_B T_S})^{-1}$ is the Fermi function containing the temperature T_S and Fermi energy ϵ_F of the source lead. Finally, ϵ_0 is the energy of the QD ground state. What eq. (3.1) essentially describes is how the QD occupation probability $P(t)$ tries to reach thermal equilibrium, $P(t) = f(\epsilon_0)$.

Using the kinetic equation (3.1) we can obtain an important expression for the capture probability $\langle N\rangle$ in an electron capture experiment that we will use throughout the rest of this work. We consider zero-temperature, $T_S = 0$, and an initially occupied QD, $P(t < t_0) = 1$, initially below the Fermi energy, $\epsilon_0(t < t_0) < \epsilon_F$. Then, at $t = t_0$ the QD is lifted out from the Fermi sea, $\epsilon_0(t > t_0) > \epsilon_F$, and the electron tunnels out with the rate $\Gamma(t)$. According to eq. (3.1) the eventual capture probability $\langle N\rangle$ of the electron in the QD is then

$$\langle N\rangle := P(t \to \infty) = e^{-\int_{t_0}^{\infty} \Gamma(t)dt} \tag{3.2}$$

For non-zero temperature, $T_S \neq 0$, the regime where eq. (3.2) still holds as a good approximation is known as the decay-cascade regime [32] which can be compared to also other physical regimes [7, 33].

Consider driving an experimental QD by applying time-dependent source and drain gate voltages $V_S(t)$ and $V_D(t)$ and then repeating the same experiment, only s' times faster, $V_S(t) \rightarrow V_S(s't)$ and $V_D(t) \rightarrow V_D(s't)$. Assuming that Γ and ϵ_0 follow the gate voltages instantaneously, $\Gamma = \Gamma(V_S, V_D)$ and $\epsilon_0 = \epsilon_0(V_S, V_D)$, implies that the tunneling integral $\int_{t_0}^{\infty} \Gamma(t)\, dt$ in eq. (3.2) decreases s' times so that the capture probabilities for the first and second scenarios, $\langle N \rangle_{s'=1}$ and $\langle N \rangle_{s'}$ respectively, are related to each other by the scaling relation

$$\langle N \rangle_{s'} = \exp\big\{ - \tfrac{1}{s'} \textstyle\int_{t_0}^{\infty} \Gamma_{s'=1}(t) dt \big\} = \langle N \rangle_{s'=1}^{1/s'}, \tag{3.3}$$

This relation will be very important for us further to develop a data-analysis technique which will be able to directly compare electron-capture data-points obtained using two different driving rates s' and to combine several curves of such data into a single curve – the master curve.

Specifically to the cubic potential model, eq. (3.3) can be rewritten without using an arbitrarily chosen reference process for which $s' = 1$:

$$\langle N \rangle = \exp\Big\{ - \frac{\omega_0}{\dot{u}} \int_{u_0}^{\infty} \Big(\frac{\Gamma}{\omega_0} \Big)\Big|_u du \Big\}, \tag{3.4}$$

Here $u_0 := u(t_0)$ is the cubic potential depth at the start of backtunneling and the role of s' to describe faster or slower driving of the system is played by the cubic potential dimensionless speed $\dot{u}/\omega_0$.

3.2. Experimental validation of the scaling relation

In this section, we demonstrate how the scaling relation (3.3) can be used on electron capture data to extract the different relative driving rates s' in the immediate vicinity of the QD and to combine all data points with different s' into a single curve – the master curve.

As our experimental data, which can be seen in fig. 3.2, we have two different datasets, both obtained from the same device, but during two different cool-downs. The temporal sequence of actions during an electron capture event is illustrated in fig. 3.1. For fig. 3.2a $V_S(t)$ changes as $\Delta V_S = -|\dot{V}_S|\Delta t$ while for fig. 3.2b $V_S(t)$ is a sinusoidal pulse characterized by a frequency f. Two experimental parameters were varied: 1) the nominal QD driving rate s, representing either $|\dot{V}_S|$ or f (the different colored curves in fig. 3.2) and 2) the time-independent gate voltage V_D (horizontal axes in fig. 3.2). Repeating the actions in fig. 3.1 periodically builds up an experimental capture probability $\langle N \rangle\big|_{V_{D,i}, s_j}$ for a pair of parameters $(V_{D,i}, s_j)$.

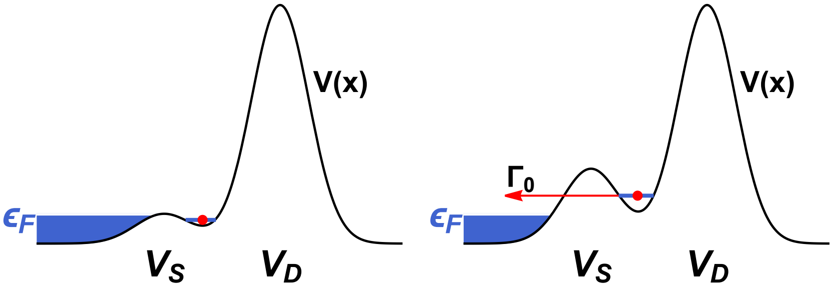

(a) Load an electron into the QD **(b)** Electron escapes by tunneling

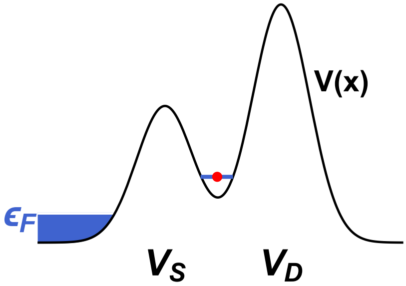

(c) Isolated QD. Electron presence detection

Figure 3.1: Illustration of the experimental protocol, 3 consecutive time-steps. Only the source gate voltage V_S is changed in time, the drain gate voltage V_D is kept fixed. **(a)** Initially, the source barrier and the QD are lowered enough in energy to load an electron into the QD. **(b)** Then, the source barrier starts rising and the electron tunnels back to the empty states of the source with a tunnel rate Γ_0. **(c)** Finally, when the source barrier is high enough and Γ_0 negligible, measurement of the presence or absence of the electron in the QD is done.

Experimentally, the relative driving rate s' in eq. (3.3) should actually be viewed as describing the immediate vicinity of the QD and not the voltages $V_S(t)$ and $V_D(t)$ programmed in a signal generator because signal distortions could be possible in intermediate filters and along transmission lines. Because of this, the values s'_j for different s_j might not be known and might have to be extracted from the data. For this, one can use the scaling relation (3.3). Plugging the experimental data $\langle N\rangle\big|_{V_{D,i},s_j}$ into it and writing $\Gamma_{s'=1}(V_D, t)$ for different drain gate voltages one can obtain

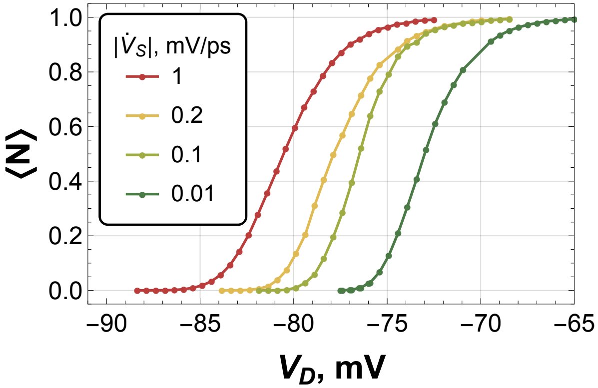

(a) During barrier rise $V_S(t) = -|\dot{V}_S|t + V_S(0)$

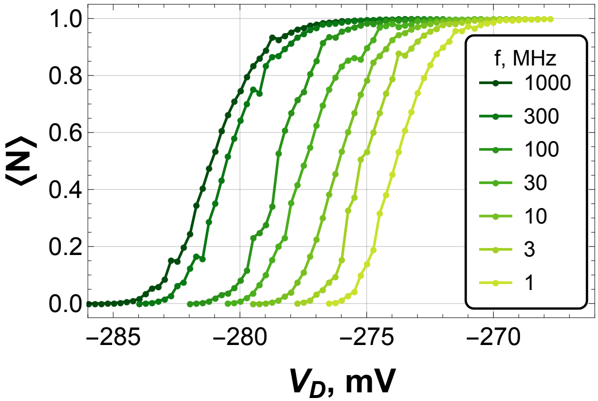

(b) During barrier rise $V_S(t) \propto \sin(2\pi f t)$.

Figure 3.2: Data from electron capture experiments as in fig. 3.1. (a) and (b) differ by the shape of $V_S(t)$. Measured quantity $\langle N \rangle$ – electron capture probability in the QD. Experimentally varied parameters – the time-independent drain gate voltage V_D and the QD closing speed $|\dot{V}_S|$ in (a) and f in (b). Electron capture is enhanced by closing the dot faster or by lowering the drain barrier (increased V_D) so that backtunneling starts at a higher source barrier.

$$\ln\big[-\ln\langle N\rangle_{V_D,\,s}\big]+\ln[s'(s)]=\ln\big[\textstyle\int_{t_0}^{\infty}\Gamma_{s'=1}(V_D,t)dt\big] \tag{3.5}$$

Thus, by sliding for each experimental s_j its double-logarithm $\ln\big[-\ln\langle N\rangle|_{V_{D,i},s_j}\big]$, plotted as a function of V_D, up by an appropriate $\ln[s'(s_j)]$ all the different experimental lines should match up with each other – a **data-collapse** should be observable – because the right-hand-side of eq. (3.5) does not depend on the driving rates s or s'. This has been done in fig. 3.3 using the shown values $s'(s_j)$ and we can observe that the data, indeed, collapses onto a single curve. We call this curve the **master curve**, write for it

$$M(V_D):=\int_{t_0}^{\infty}\Gamma_{s'=1}(V_D,t)dt, \tag{3.6}$$

and note that its value M characterizes the conditions during an electron capture process assuming a fixed QD driving rate $s'=1$.

We view the observed data-collapse in fig. 3.3 as evidence that the experimental system has been operated in the decay-cascade regime where eq. (3.2) holds and evidence that the time-dependent tunneling rate function can be experimentally scaled along the time axis, $\Gamma(t)\to\Gamma(s't)$, simply by applying the same source gate voltage pulse faster or slower.

Performing a data-collapse with experimental capture probabilities $\langle N\rangle|_{V_{D,i},s_j}$ as in fig. 3.3 has several experimentally practical benefits: first, the relative driving rates s'_j which characterize the vicinity of the QD can be estimated and, second, the range of drain gate voltages V_D covered by the master curve is larger than any range of V_D covered by probabilities $\langle N\rangle|_{V_{D,i},s_j}$ only corresponding to a single driving rate s_j. This is important because it allows probing the escape mechanism of the electron over a larger parameter range.

The appearance of a master curve $M(V_D)$ in both datasets motivates its further theoretical study – we can ask, what determines its precise shape. For example, the phenomenological model of eq.'s (1.1a) and (1.1b) which have ϵ_0 and $\ln\Gamma$ that are linear in gate voltages gives a linear $\ln M(V_D)$ which does not entirely fit with fig. 3.3, especially with fig. 3.3b. This gives us an opportunity to study shallow QDs and electron capture processes within them with greater detail. For this, we will use the microscopic one-dimensional cubic potential model whose state-dependent master curve can be written, from eq. (3.7), as

$$M_n(u_0):=\int_{u_0}^{\infty}\left(\frac{\Gamma_n}{\omega_0}\right)\Big|_u du \tag{3.7}$$

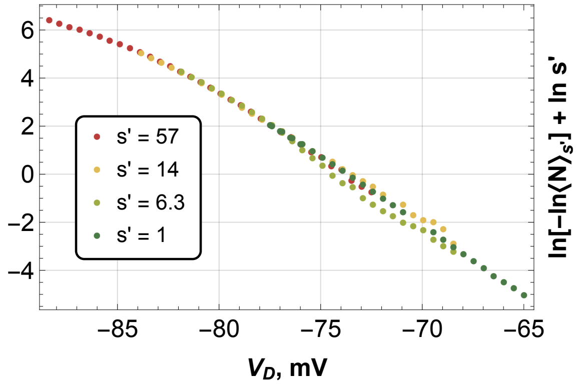

(a) Linear $V_S(t)$.

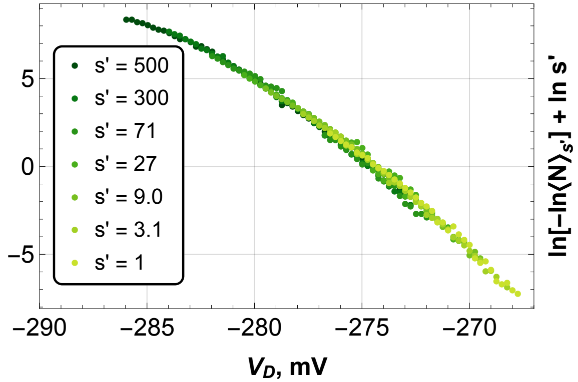

(b) Sinusoidal $V_S(t)$.

Figure 3.3: Data-collapse onto a single master curve. Using eq. (3.5) and appropriately extracted relative driving speeds $s'(s_j)$ data obtained at different nominal driving rates s can be aligned into a single curve.

3.3. Tunnel rates out of the cubic well

In this section, to compare the cubic model to the electron capture data in fig.'s 3.2 and 3.3 we compute the cubic potential tunnel rates $\Gamma_n(u)$ necessary for the capture probability prediction, eq. (3.4). On the way, we also compute the corresponding resonance energies $E_n(u)$. For this, we use 3 different methods – asymptotic expressions from perturbation theory, the WKB (Wentzel-Kramers-Brillouin) approximation and the complex scaling method. While the first two methods are approximations we regard the values given by complex scaling as precise and only limited by the numerical nature of the method.

We start by simply quoting from [34] the asymptotic expressions for the case of a deep well, $u \to \infty$. The lowest order terms in $u^{-1/2}$ for $\Gamma_n(u)$ and $E_n(u)$ are

$$\Gamma_n^{\mathrm{PT}}/\omega_0 = \frac{6^{3/2}}{\sqrt{\pi}} \frac{432^n}{n!} u^{n+1/2} e^{-36u/5} \tag{3.8a}$$

$$E_n^{\mathrm{PT}} = \hbar\omega_0(n + 1/2) \tag{3.8b}$$

We see that the perturbative tunnel rates Γ_n^{PT} vanish exponentially with an increasing depth u and that the perturbative energies E_n^{PT} are simply the harmonic oscillator energies.

Next, we explain how $\Gamma_n(u)$ and $E_n(u)$ can be calculated using the WKB (Wentzel-Kramers-Brillouin) approximation [35]. For this, we first define an energy dependent dimensionless classical phase space area

$$a(E) := \frac{1}{\pi\hbar} \int_{x_2(E)}^{x_3(E)} \sqrt{2m(E - V(x))}dx \tag{3.9}$$

which gives the classical phase space area, in units of $2\pi\hbar$, enclosed by a classical oscillatory trajectory with energy E. Here x_2 and x_3 are the boundaries of the classically allowed well region for this energy, $V(x_{2,3}) = E$. With this, the WKB energy quantization condition can be written simply as

$$a\big(E_n^{\mathrm{WKB}}\big) = n + 1/2 \quad , \quad n = 0, 1, 2... \tag{3.10}$$

and interpreted to say that each quantized energy E_n^{WKB} encloses a half-integer area, in units of $2\pi\hbar$, of classical phase space. Thus, it is like each consecutive energy eigenstate occupies its own region of phase space with area $2\pi\hbar$ – its own **quantum of phase space**.

The WKB expression for the discrete tunnel rates is

$$\Gamma_n^{\mathrm{WKB}} = \frac{1}{\tau(E_n^{\mathrm{WKB}})} \exp\Big[-\frac{2}{\hbar} \int_{x_1(E_n^{\mathrm{WKB}})}^{x_2(E_n^{\mathrm{WKB}})} \sqrt{2m\big(V(x) - E_n^{\mathrm{WKB}}\big)}dx \Big] \tag{3.11}$$

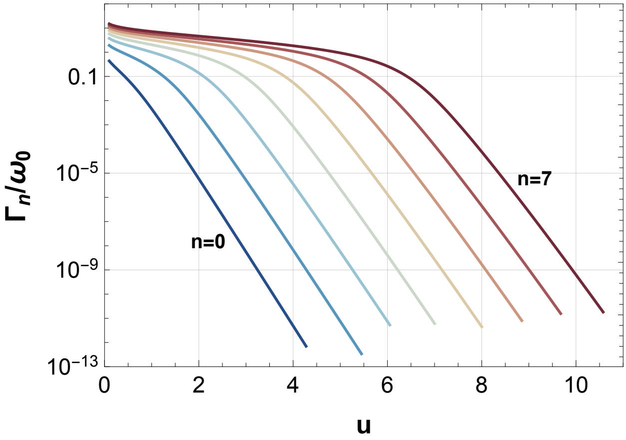

(a) Tunnel rates $\Gamma_n(u)$.

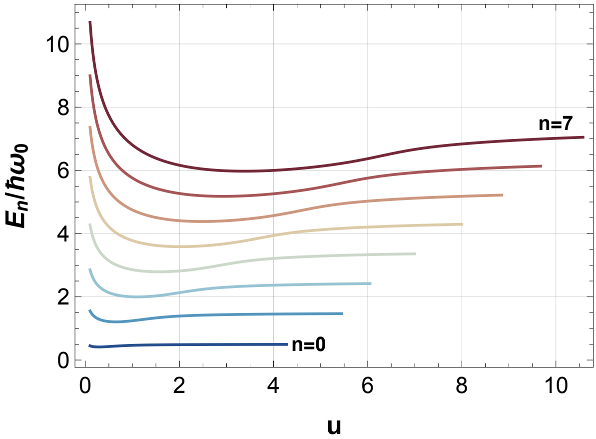

(b) Energies $E_n(u)$.

Figure 3.4: Results of the complex scaling method: calculated tunnel rates $\Gamma_n(u)$ and energies $E_n(u)$ for the 8 lowest resonances in the cubic potential, $n = 0, 1 \ldots 7$. Results are shown for depths u where the relative error of the numeric calculation is below 10^{-4} for the tunnel rates Γ_n.

where $\tau(E)$ is the energy-dependent classical oscillation period, the factor with the exponential – the WKB transmission probability over the barrier and $x_{1,2}$ – the boundaries of the classically forbidden barrier region, $V(x_{1,2}) = E$. To actually use eq. (3.11) we have found the functions $a(E)$ and $\tau(E)$ specific to the cubic potential,

$$a(E) = u\,\frac{E}{V_b} \cdot {}_2F_1\Big(\frac{1}{6}, \frac{5}{6}, 2, \frac{E}{V_b}\Big) \tag{3.12a}$$

$$\tau(E) = \frac{2\pi}{\omega_0}\,{}_2F_1\Big(\frac{1}{6}, \frac{5}{6}, 1, \frac{E}{V_b}\Big), \tag{3.12b}$$

where ${}_2F_1(...)$ is the hypergeometric function. Eq. (3.12a) can also be used for the integral in (3.11) due to the symmetry of the cubic potential, $V(x) = V_b - V(-x)$. The oscillation period $\tau(E)$ starts at the quadratic approximation value, $\tau(0) = 2\pi/\omega_0$, then gradually increases while remaining with $2\pi/\omega_0 < \tau(E) < 3\pi/\omega_0$ over almost all energies in the well until at the very top of the barrier, $E \to V_b$, $\tau(E)$ diverges logarithmically as for a quadratic barrier. The phase space area $a(E)$, being proportional to the integral of $\tau(E)$, stays close to the quadratic approximation baseline $u\,E/V_b$ and differs from it slightly only at the highest energies. Its maximal value is the full phase space area of the QD, $a(V_b) = 18u/5\pi$.

The last method that we use for obtaining $\Gamma_n(u)$ and $E_n(u)$ is the complex scaling method [34, 36]. It requires diagonalizing a dimensionless non-hermitean Hamiltonian

$$\frac{\mathcal{H}_\theta(u)}{\hbar\omega_0} = \frac{\hat{\mathrm{p}}^2}{2} e^{-2i\theta} + \frac{\hat{\mathrm{x}}^2}{2} e^{2i\theta} + \frac{\hat{\mathrm{x}}^3}{3\sqrt{6u}} e^{3i\theta} \tag{3.13}$$

which contains the dimensionless coordinate $\hat{\mathrm{x}}$ and momentum $\hat{\mathrm{p}}$ and which depends on an extra parameter θ. By finding complex eigenvalues which, on certain intervals, do not depend on θ one has obtained $\big(E_n/\hbar\omega_0 - i\Gamma_n/2\omega_0\big)$. We have done this by numerical diagonalization after expanding $\mathcal{H}_\theta(u)$ as a finite matrix in the harmonic oscillator basis. The results of this calculation can be seen in fig. 3.4.

We compare the results from the three different calculation methods in fig. 3.5. Fig. 3.5a shows the tunnel rates and fig. 3.5b – the energies. Dark-blue curves correspond to the precise functions $\Gamma_n(u)$ and $E_n(u)$ obtained using complex scaling, dark-green curves – to asymptotic expressions and light-green curves – to WKB. The vertical gridlines mark the depths u at which a discrete energy exits or enters the well, $E_n(u) = V_b$, and the horizontal gridlines mark $\Gamma_n/\omega_0 = 1/4\pi$ in fig. 3.5a, which we explain later, while in fig. 3.5b they mark the harmonic oscillator energies $E_n = \hbar\omega_0(n + 1/2)$.

First of all, we observe that the precise tunnel rates and energies are consistent with the perturbation theory asymptotic expressions, eq.'s

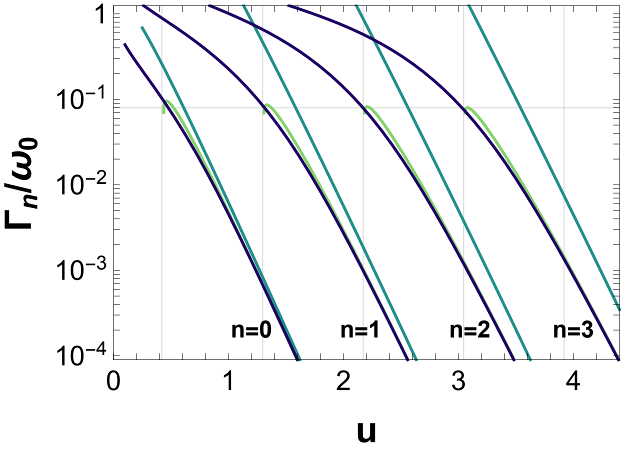

(a) Tunnel rates $\Gamma_n(u)$.

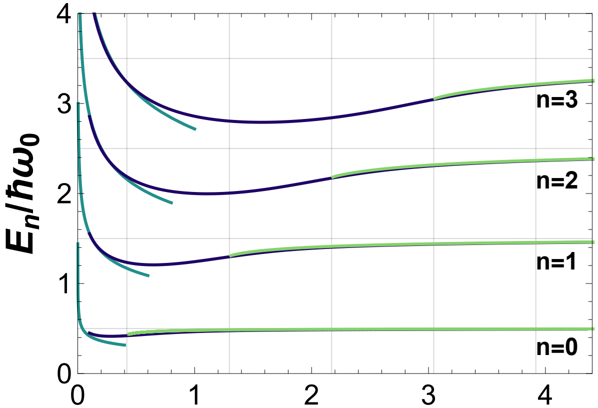

(b) Resonance energies $E_n(u)$.

Figure 3.5: Tunnel rates $\Gamma_n(u)$ and energies $E_n(u)$ of the cubic potential resonances as a function of the dimensionless depth u. Various colours correspond to various methods of computation: dark-blue – exact functions computed using the complex scaling method, light-green – the WKB approximation and dark-green – asymptotic expressions. Vertical gridlines mark the appearence / disappearence of another discrete energy in the well, $E_n = V_b$. The horizontal gridline in (a) marks $2\pi\Gamma_n/\omega_0 = 1/2$ which can loosely be interpreted as corresponding to half-transmission probability over the barrier and in (b) the horizontal gridlines mark $E_n = \hbar\omega_0(n+1/2)$.

(3.8a) and (3.8b). In fig. 3.5a, at large u the dark-blue curves gradually approach the dark-green curves, eq. (3.8a), so that the precise tunnel rates $\Gamma_n(u)$ really decay exponentially with u with the characteristic exponent $(-36u/5)$. Similarly, in fig. 3.5b at large u the precise energies $E_n(u)$ in dark blue approach their corresponding limiting values – the harmonic oscillator energies $\hbar\omega_0(n+1/2)$. However, it is also visible that the convergence of $\Gamma_n(u)$ and $E_n(u)$ to their large-u asymptotic expressions becomes slower with increasing n. Thus, the asymptotic expressions (3.8a) and (3.8b) should be best used not just at large depths below the barrier (roughly, large $u-n$) but at large depths with respect to the whole energy range of the well, $n/u \ll 1$. Fig. 3.5b, additionally, shows consistency between the precise and asymptotic energies (dark-green curves, not given by an equation in the text) in the shallow regime, $u \to 0$. The apparent divergence is only due to the vanishing frequency $\omega_0 = u^{1/5}\Omega_b \to 0$ in this regime, the functions $E_n(u)/\hbar\Omega_b$ and $\Gamma_n(u)/\Omega_b$ remain finite at $u = 0$.

Turning now to the WKB tunnel rates and energies, $\Gamma_n^{WKB}(u)$ and $E_n^{WKB}(u)$ – the light green curves in fig. 3.5 – we see that, while increasing u, they converge to the precise functions $\Gamma_n(u)$ and $E_n(u)$ faster than the corresponding large-u asymptotics. Thus, for higher states n and in situations where $n/u \ll 1$ is not yet satisfied and $n \sim u$ is more the case the WKB approximated rates and energies might be preferred over the asymptotic expressions. Looking at fig. 3.5b we see that over their whole range of existence the WKB energies $E_n^{WKB}(u)$ match with the precise functions $E_n(u)$ remarkably well and also the appearance of resonances, $E_n(u) = V_b$, (marked by the vertical gridlines) is predicted by the WKB energies very precisely. For the WKB tunnel rates, a slight caveat of the functions $\Gamma_n^{WKB}(u)$ is their slightly wrong exponential prefactor in the $u \to \infty$ limit, for example, $\lim_{u\to\infty}\Gamma_0^{WKB}/\Gamma_0^{\mathrm{PT}} = \sqrt{e/\pi} \approx 0.93$. However, this mismatch decreases for increasing n. The second disadvantage of the WKB rates is their unphysical vanishing at the top of the barrier, $E_n \to V_b$, which is due to the diverging classical oscillation period $\tau(E)$ at $E \to V_b$.

From the above, we see that at energies at the top of the barrier, $E_n = V_b$ and slightly below, neither the asymptotic expressions nor the WKB approximation faithfully reproduce the precise tunnel rates $\Gamma_n(u)$. Because of this, the results of the complex scaling method are most significant and practically important in precisely this – the highly non-perturbative – regime. Even more, looking at fig. 3.5 we see that the precise tunnel rates and energies supplied by complex scaling extend even above the barrier, $E_n > V_b$. We will use this later for describing thermally enhanced electron escape to continuously connect escape rate contributions from the discrete resonances below the barrier to the contribution from the continuum above. For a physical interpretation of the $E_n \approx V_b$

regime, we see that all levels, when they reach the top of the barrier (vertical gridlines), all have approximately the same tunnel rate $\Gamma_n/\omega_0 = 1/4\pi$ (horizontal gridline in fig. 3.5a). Roughly interpreting $2\pi\Gamma_n/\omega_0$ as the quantum transmission probability through the barrier this corresponds to a transmission probability of 1/2.

Overall, the cubic potential tunnel rate and energy functions $\Gamma_n(u)$ and $E_n(u)$ obtained here will be highly valuable tools in the following sections and chapters. Almost all of the subsequent main results will use them. We have used the values obtained by complex scaling whenever we had them and the asymptotic expressions (3.8a) and (3.8b) otherwise. In the logical structure of this work these functions will be one of the most direct ways through which the cubic potential assumption enters our calculations as, otherwise, we do not actually solve the corresponding Schrodinger equation (2.7).

3.4. Experimental validation of the cubic model

In this section, we compare the cubic potential model with the electron capture data presented above through their respective master curves – fig. 3.3 for the data and eq. (3.7) applied to the ground state, $n = 0$, for the model. For both datasets, we find good agreement which lets us further characterize the experimental system in terms of cubic model quantities – the depths u_0 at the start of backtunneling and dimensionless driving speeds $\dot{u}/\omega_0$. We then discuss the observed agreement as experimental evidence for the cubic model and, finally, we draw broader conclusions from the whole chapter 3.

To do the comparison between the model and data one first has to compute the cubic potential master curves $M_n(u_0) := \int_{u_0}^{\infty} (\Gamma_n/\omega_0)\, du$. We do this for several of the lowest resonances by numerically integrating the dimensionless tunnel rate functions $(\Gamma_n/\omega_0)|_u$ from sec. 3.3 and fig. 3.5a. We show the results for the 4 lowest resonances, $n = 0, 1, 2, 3$, in fig. 3.6. In this section, we will only need the ground state master curve but in the following chapters also excited state master curves will be necessary. As can be seen from fig. 3.6, the master curves look qualitatively quite similar to their corresponding tunneling rate functions Γ_n/ω_0: for large u_0 they all decay roughly exponentially as $e^{-36u_0/5}$ while around and above $E_n \approx V_b$ they show a slightly milder exponential decay.

The last thing necessary for a comparison between our model and the data is a relation $u_0(V_D)$ in $M_0(u_0)$ between the initial cubic potential depth u_0 and the experimental time-independent gate voltage V_D. For this, we make two linearity assumptions: 1) the cubic potential parameters b

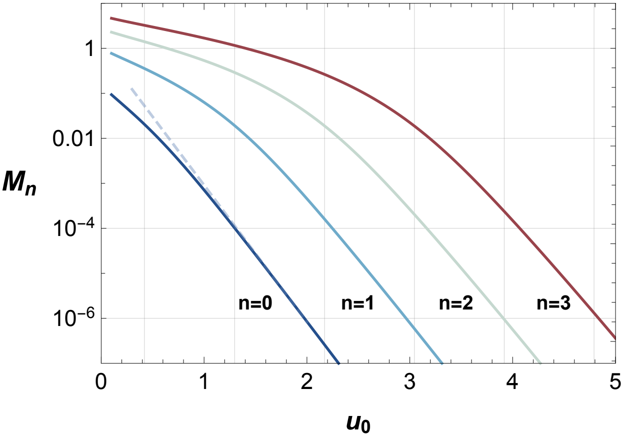

Figure 3.6: Four lowest master curves $M_n(u_0) = \int_{u_0} (\Gamma_n/\omega_0) du$. The dashed line makes the slight non-linearity of $\ln M_0(u_0)$ more apparent. Vertical gridlines mark the appearence / disappearence of another discrete energy in the well, $E_n = V_b$.

and F depend on the gate voltages as

$$b\,(V_S, V_D) = b \tag{3.14a}$$

$$\Delta F(V_S, V_D) = \alpha_S^{(F)} \Delta V_S + \alpha_D^{(F)} \Delta V_D, \tag{3.14b}$$

from which the time-dependence $F(t) = \dot{F}t$ and $b(t) = \text{const}$ in $\mathcal{H}(t)$ then follows, and 2) the condition $\epsilon_0 = \epsilon_F$ – the QD energies cross the Fermi energy – is satisfied on a straight line $V_S^{\epsilon_F}(V_D)$ in the voltage map (V_D, V_S), see fig. 3.7. This gives linearity between $F(t_0)$ and V_D which, through eq. (2.3), results in

$$u_0(V_D) = [\tilde{\alpha}(V_D - V_D^c)]^{5/4}, \tag{3.15}$$

where V_D^c and $\tilde{\alpha}^{-1}$ are two arbitrary voltages which will become fit parameters shortly. Comparing these assumptions with previous works the approach here can be seen as linearizing $\epsilon_0(V_S, V_D)$, eq. (1.1a), which has been done previously [7, 8]. Moreover, we additionally assume an extremely strong dependence of ϵ_0 on V_S such that no other effect (like the time-dependent crossing of the energy level $\epsilon_0(t)$ and the temperature-smeared Fermi step $\epsilon_F \pm k_B T_S$) can compete with it. However, for the tunnel rate Γ we do not directly linearize $\ln\Gamma$. Instead, we linearize in eq. (3.14b) the parameter F of the cubic potential and then obtain the corresponding tunnel rates $\Gamma_0(V_S, V_D)$ through the results of sec. 3.3. This gives a qualitatively exponential $\Gamma_0(V_S, V_D)$ but predicts deviations from

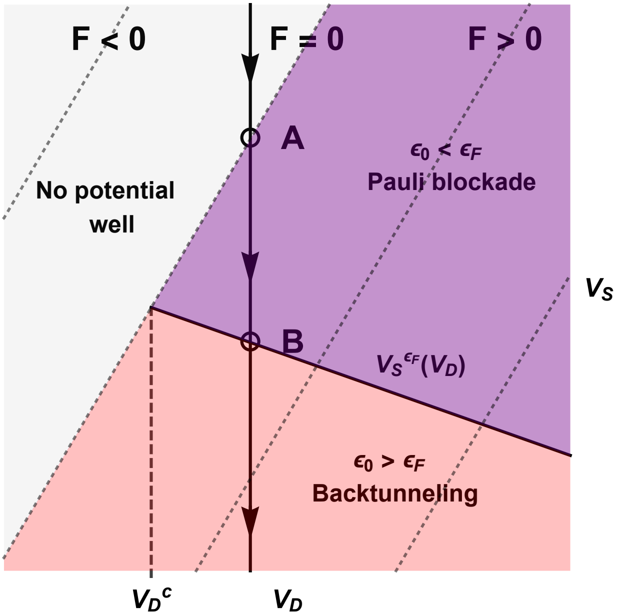

Figure 3.7: The voltage map (V_D, V_S) motivating the assumption for $u_0(V_D)$. $F(V_D, V_S)$, which is assumed linear, is represented by the short dashed lines. In the grey region the cubic potential has no confining well due to $F < 0$. A cubic QD exists in the purple and pink regions where $F > 0$. We assume the emergence of the QD from the Fermi sea, $\epsilon_0 = \epsilon_F$, on the solid straight line $V_S^{\epsilon_F}(V_D)$. The vertical line with arrows represents the time dependence of voltages during an experiment. Point A marks the appearence of a cubic QD and point B marks the start of electron backtunneling which coincides with $t = t_0$. Combining linearity of $F(V_D, V_S)$ and $V_S^{\epsilon_F}(V_D)$ with $u \propto F^{5/4}$ gives eq. (3.15).

this simple dependence at small depths u (fig. 4.6) or over larger intervals of u (eq.'s (3.8a), (2.3) and (3.14b) combined).

Turning now to the fit between $M_0(u_0(V_D))$ and the data we have 3 fit parameters: V_D^c, $\tilde{\alpha}$ and $(\dot{u}/\omega_0)/s'$. The significance of the critical drain gate voltage V_D^c (see fig. 3.7, the vertical dashed line) is that for $V_D < V_D^c$ the energies of the QD, when it has formed, will already be higher than the Fermi energy ϵ_F so that capture of electrons in the QD will become highly ineffective. The second parameter, $\tilde{\alpha}$, corresponds to a voltage scale $\tilde{\alpha}^{-1}$ for: 1) the capture probability step $\langle N \rangle = 0 \rightarrow 1$ and 2) significant changes of the depth u of the cubic QD. The third parameter, the ratio $(\dot{u}/\omega_0)/s'$, corresponds to replacing the relative driving rate s' whose definition depended on an arbitrarily chosen reference charging process with the microscopic driving speed $\dot{u}/\omega_0$ which has a clear physical interpretation. Using $(\dot{u}/\omega_0)/s'$ one can slide all the experimental points in fig.'s 3.3a or 3.3b uniformly up or down to match them with $\ln M_0\big([\tilde{\alpha}(V_D - V_D^c)]^{5/4}\big)$. The fit results can be seen in fig.'s 3.8a and 3.8c where, to be precise, the parameters have been used to minimize the mean squared distance between $\ln M_0\big([\tilde{\alpha}(V_D - V_D^c)]^{5/4}\big)$ from the model and $\ln\big[-s'(s_l)\ln\langle N\rangle|_{V_{D,i},s_l}\big] + \ln\big[(\dot{u}/\omega_0)/s'\big]$ from data. Essentially, this maximizes the visual match between the model (red curves) and data as seen in fig.'s 3.8a and 3.8c. We view the obtained fits as good and take them as evidence that the simple one-dimensional cubic potential model can, indeed, describe experimental quantum dots and that they can reach the shallow regime at which this is expected.

From these fits one can obtain two valuable relations from experimental to microscopic quantities. First, one obtains the function $u_0(V_D)$ which gives, for each time-independent drain gate voltage V_D, the approximate number u_0 of confined quantum states in the QD while it emerges from the Fermi sea, $\epsilon_0 = \epsilon_F$. Looking at the upper horizontal axes in fig.'s 3.8a and 3.8c we see that in both experiments $u_0 < 3$ so that both of them have, indeed, been performed in the shallow regime of just a couple of discrete confined states. The second relation that we obtain from the fit of data to the master curve $M_0(V_D)$ is the relation from the experimental nominal driving rates s – either frequency or linear ramp rate – to the cubic model driving rates $\dot{u}/\omega_0$. We have plotted this relation for the nominal ramp rates s_l present in both datasets in fig.'s 3.8b and 3.8d from which we see that both experiments have stayed below the driving rate $\dot{u}/\omega_0 = 10^{-2}$. This means that experimentally the rate of change $\dot{u}$ of the external conditions for the electron has not been able to "outpace" the electron itself, its small oscillation frequency ω_0. This is actually a self-consistency condition on the analysis done here using the ground state master curve $M_0(V_D)$. Because at $\dot{u}/\omega_0 \sim 1$ one expects that non-adiabatic transitions between

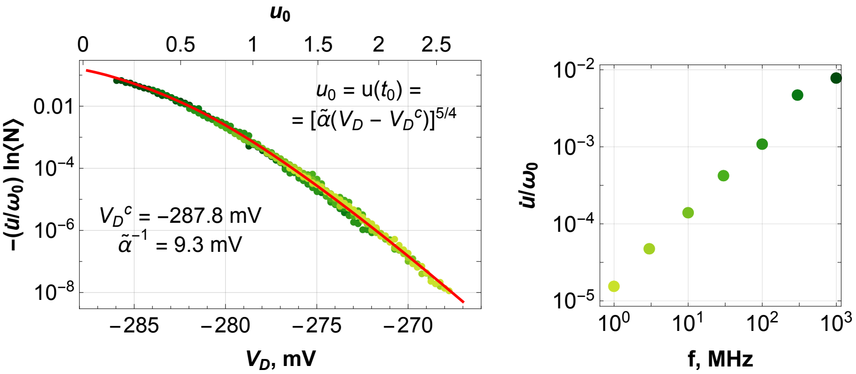

(a) Sinusoidal $V_S(t)$. **(b)** Sinusoidal $V_S(t)$.

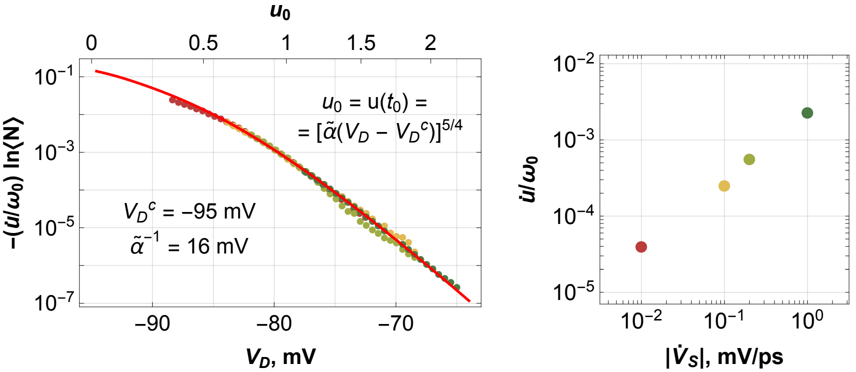

(c) Linear $V_S(t)$. **(d)** Linear $V_S(t)$.

Figure 3.8: (a), (c) – fits of the cubic potential ground state master curve $M_0\big([\tilde{\alpha}(V_D - V_D^c)]^{5/4}\big)$, depicted as the red curves, to the experimentally obtained master curves of fig. 3.3. (b), (d) – the corresponding inferred microscopic driving rates $\dot{u}/\omega_0$ for each of the experimental nominal driving rates f or $|\dot{V}_S|$. Using the fit parameters V_D^c and $\tilde{\alpha}$ a relation is obtained between the experimental drain gate voltage V_D and the microscopic depth $u_0 = u(t_0)$ at the start of electron backtunneling, see the upper / lower horizontal axes in (a) and (c).

the discrete quantum states n will start becoming significant so that the assumption of the electron tunneling out from the QD exclusively from the ground state would no longer hold.

We review briefly the ways by which the cubic potential assumption determines the exact shape of the model curve $\ln[M_0(V_D)]$. First, the overall shape of $\ln[M_0(V_D)]$ is mainly determined by the relation $u_0(V_D) = [\tilde{\alpha}(V_D - V_D^c)]^{5/4}$. This relation was obtained from two linearity assumptions on the gate voltages V_S and V_D, however, the specific power $5/4$ in $u_0(V_D)$ was not guessed or fitted, it was derived from eq. (2.3) of the cubic potential model. The second way through which the cubic potential assumption determines the precise shape of $\ln[M_0(V_D)]$ is through the slight non-linearity of $\ln[M_0(u_0)]$ at small depths, $u_0 \lesssim 1$, shown in fig. 3.6. This is a direct consequence of the precise ground state tunnel rates $\Gamma_0(u)$ of the cubic potential.

We list now the main achievements of this chapter:

- We have demonstrated that the idea of a master curve, based on a kinetic equation model in the zero-temperature limit on the lead, can be used in practice to simplify electron capture data analysis and directly compare capture probabilities determined by tunnel rates which differ by several orders of magnitude. With the empirically obtained master curve we are able to probe the escape mechanism of the electron over a larger range of physical conditions with less experimental effort.

- With the data-collapse procedure, represented by eq. (3.5), we have given a practical method for estimating the actual response of an experimental QD to variations in the rate by which the nominal input voltage signal is varied. More concretely, we can provide a function $s'(s)$ which tells how the driving rate s' at the vicinity of the QD changes as the nominal driving rate s set by the signal generator is changed.

- By comparing the experimentally obtained master curves (fig. 3.3) with the cubic potential ground state master curve $M_0(u_0)$ we have gained access to the microscopic quantities u_0 and $\dot{u}/\omega_0$ and their relation to the corresponding experimentally tuneable parameters. This microscopic knowledge can be used to predict the speed-limits for the operation of tuneable barrier QD based devices and also to understand the reason for the corresponding breakdown of operation at these limits. That is, we can predict from experimental data which will happen first while increasing the operation frequency – either non-adiabatic excitations will start playing a role or the confining well under the Fermi energy will disappear completely.

Thus, we view the one-dimensional cubic model as a significant step forward in the modelling of tuneable barrier QD based devices. Because, in contrast to it, the sofar other alternative successful models, like the decay-cascade model [32], have only been phenomenological and lacking important microscopic details. At this point, one possible important future research direction would be be testing the universality hypothesis – that this model is general enough to describe many different experimental devices in their shallow regime. This would require performing similar experiments and analysis on the obtained data as presented in the current chapter 3 with many other experimental tuneable barrier QD devices. However, in this thesis we pursue another direction – in the following chapters we develop alternative tests for the one-dimensional cubic potential hypothesis in more complicated physical conditions – non-zero temperature and non-zero magnetic field.

4. TEMPERATURE IN THE QUANTUM DOT

In this chapter, we turn to considering temperature effects in shallow QDs. Two different temperature regimes for electron escape are possible depending on which escape mechanism is dominant – quantum tunneling or thermally activated classical escape, both illustrated in fig. 4.1. In sec. 4.1 we consider a static cubic QD; we adapt ideas from transition state theory [37] to our case of just a couple of discrete states in the QD to formulate an escape rate $\langle \Gamma(u) \rangle_{k_B T}$ which correctly describes the two different regimes as well as the crossover between them. In sec. 4.2 we turn to the time-dependent scenario of electron capture; in our model predictions for the capture probabilities we observe a similar temperature behavior as for the escape rates from a static potential – thermal activation above a certain crossover temperature. Comparing this to the qualitatively same behavior in experimental data leads us to the main results of this chapter – estimation of the cubic potential energy scale $\hbar\Omega_b$ and, consequently, any other quantity of the cubic model in the experimental system.

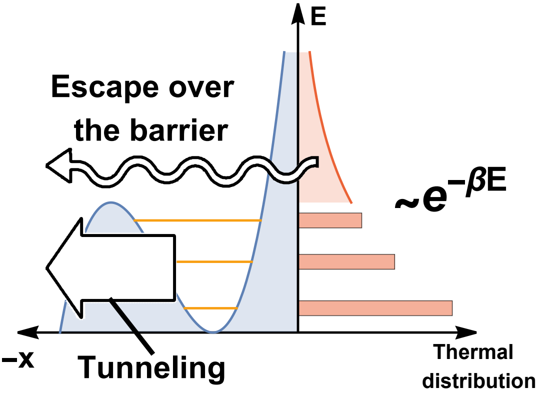

Figure 4.1: Two escape mechanisms out from the QD induced by temperature $T = 1/k_B\beta$: quantum tunneling with energies below the barrier, $E < V_b$, and classical escape with energies above the barrier, $E > V_b$, excited due to thermal fluctuations. Observing a crossover between the temperature regimes where one mechanism dominates or the other can help determine energetic parameters of the confining potential – its level spacing $\hbar\omega_0$ or the energy scale $\hbar\Omega_b$ of the cubic potential.

4.1. Thermal escape from a static cubic well

In this section, we present our model for the temperature-dependent escape rate $\langle\Gamma(u)\rangle_{k_BT}$ from a static cubic well. To correctly connect contributions from tunneling, $E < V_b$, and thermally induced classical escape, $E > V_b$, we use the idea of the phase space quantum from WKB approximation. We then validate the obtained rate $\langle\Gamma(u)\rangle_{k_BT}$ by comparing it to known results from classical transition state theory [37] as well as experimental data from superconducting physics [30, 31].

We start by writing the escape rate $\langle\Gamma(u)\rangle_{k_BT}$ as a thermal average over energy-dependent escape rates $\Gamma(u, E)$,

$$\langle\Gamma(u)\rangle_{k_BT} = Z^{-1}(u,\beta)\int_0^\infty \Gamma(u,E)\rho(u,E)e^{-\beta E}dE \tag{4.1a}$$

$$Z(u,\beta) = \int_0^\infty \rho(u,E)e^{-\beta E}dE, \tag{4.1b}$$

where $\rho(u, E)$ is the density of states in the QD region, $x > -x_0$. As we will use a different $\rho(u, E)$ for each of the energy ranges $E < V_b$, $E \approx V_b$ and $E > V_b$ we split both $\langle\Gamma\rangle_{k_BT}$ and Z into 3 corresponding terms:

$$\langle\Gamma\rangle_{k_BT} = \langle\Gamma\rangle_{\text{res}} + \langle\Gamma\rangle_{\text{tr}} + \langle\Gamma\rangle_{\text{cont}} \tag{4.2a}$$

$$Z = Z_{\text{res}} + Z_{\text{tr}} + Z_{\text{cont}} \tag{4.2b}$$

For the tunneling contribution, $E < V_b$, $\rho(u, E)$ is a sum of delta functions each located at the resonant energies $E_n(u)$ of the cubic well computed in sec. 3.3. The corresponding rates are the discrete $\Gamma_n(u)$'s

$$\langle\Gamma\rangle_{\text{res}} = Z^{-1}\sum_{n=0}^{n_b-1} e^{-\beta E_n}\Gamma_n \tag{4.3a}$$

$$Z_{\text{res}} = \sum_{n=0}^{n_b-1} e^{-\beta E_n} \tag{4.3b}$$

Here, with $n_b := \lfloor a(V_b)\rfloor = \lfloor 18u/5\pi\rfloor$ summation is done only over resonances with a full phase space quantum in the QD, see fig. 4.2.

For the contribution $\langle\Gamma\rangle_{\text{cont}}$ at energies above the barrier, $E > V_b$, we use for $\rho(E)$ an approximate continuum version of eq. (3.10), $\rho(E) = \frac{da}{dE} = \frac{\tau(E)}{2\pi\hbar}$, which still assumes a single quantum state per phase space region with area $2\pi\hbar$. Here, $a(E)$ is in fig. 4.2 the area enclosed by the spatial boundary of the QD, $x = -x_0$, and the classical, free trajectory with energy E. $\tau(E)$ is the time spent in the QD by such a free classical particle. For $\Gamma(E)$ we use $\Gamma(E) = \frac{\mathcal{T}(E)}{\tau(E)}$ where $\mathcal{T}(E) = [1 + \exp\{-2\pi(E - V_b)/\hbar\omega_0\}]^{-1}$ is the quantum transmission probability above the barrier

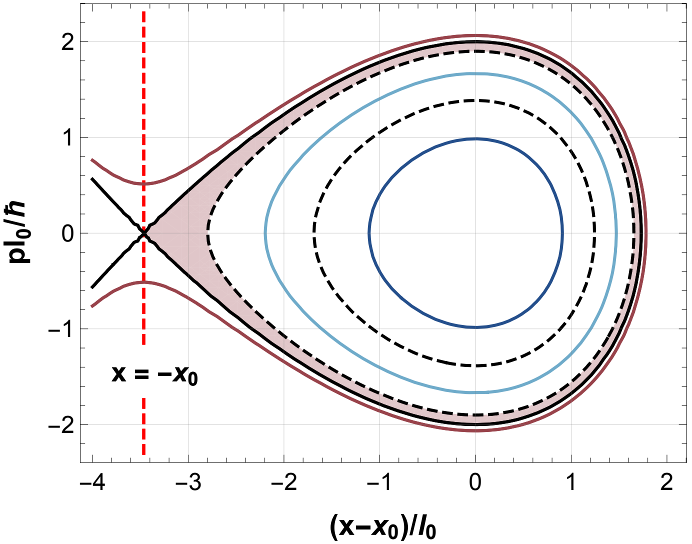

Figure 4.2: Horizontal and vertical axes – dimensionless coordinate and momentum axes of classical phase space. $l_0 := \sqrt{\hbar/m\omega_0}$ is the quantum harmonic oscillator spatial localization scale. The classically confined phase space region of the cubic potential is encircled by the solid black line, $p^2/2m + V(x) = V_b$. Light-blue, dark-blue and dark-red curves – the cubic potential resonance energy level-lines $p^2/2m + V(x) = E_{0,1,2}(u)$. The corresponding full phase space quanta (for $n = 0, 1$) are enclosed by the black dashed curves. For the presented depth $u = 2$ there is a fractional phase space quantum in the QD, shaded in light-red, corresponding to $a_{n_b}(u) \neq 0$ and a not yet completely formed new resonance $n_b = 2$.

using its quadratic approximation. Thus,

$$\langle\Gamma\rangle_{\text{cont}} = \int_{V_b}^{\infty} \mathcal{T}(E) e^{-\beta E} \frac{dE}{2\pi\hbar Z} \tag{4.4}$$

In the classical limit $\hbar\omega_0 \ll k_B T \ll V_b$ this simplifies because $\mathcal{T} \approx 1$ on the thermal energy scale $k_B T$ and $Z \approx Z_{\text{res}} \approx k_B T/\hbar\omega_0$. Then

$$\langle\Gamma\rangle_{\text{cont}} \approx \Gamma_{\text{cl}} = \frac{\omega_0}{2\pi} e^{-V_b/k_B T} \tag{4.5}$$

where the second equation is a result from classical transition state theory [37]. For the continuum contribution Z_{cont} to the partition function Z we compute it as an integral over classical phase space using $\frac{da}{dE} dE =$

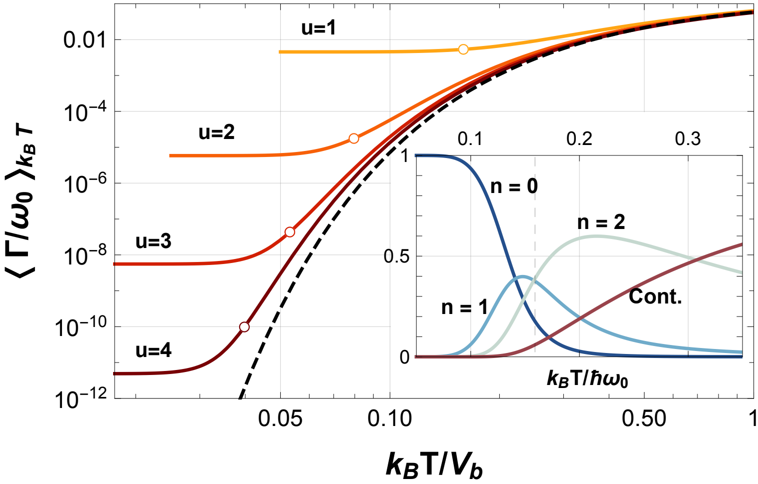

Figure 4.3: Coloured curves, yellow to dark-red, give the computed temperature dependent thermal escape rates $\langle\Gamma\rangle_{k_BT}$ for consecutive depths $u = 1, 2, 3, 4$. The black dashed curve gives the classical thermal escape rate $\Gamma_{\mathrm{cl}} = \omega_0\, e^{-\beta V_b}/2\pi$. The open circles mark for each depth its crossover temperature $k_B T_0 = \hbar\omega_0/2\pi$ which roughly separates the quantum ground state tunneling regime, $\langle\Gamma\rangle_{k_BT} \approx \Gamma_0(u)$, from the classical thermal escape regime, $\langle\Gamma\rangle_{k_BT} \approx \Gamma_{\mathrm{cl}}$. Inset: escape mechanism crossover. The vertical axis gives the relative contributions to $\langle\Gamma\rangle_{k_BT}$ of the discrete states, $\Gamma_n\, e^{-E_n/k_BT}/Z\langle\Gamma\rangle_{k_BT}$, and the continuum, $\langle\Gamma\rangle_{\mathrm{cont}}/\langle\Gamma\rangle_{k_BT}$, for the case of exactly 3 resonances in the cubic QD, $u = 15\pi/18$. Around the crossover temperature, marked by the vertical dashed gridline, the main weight of $\langle\Gamma\rangle_{k_BT}$ shifts from the ground state, $n = 0$, through the excited states, $n = 1, 2$, to the continuum.

$\frac{dxdp}{2\pi\hbar}$ and, further,

$$\begin{aligned} Z_{\mathrm{cont}} &= \int_{\substack{E>V_b,\\ x>-x_0}} e^{-\beta\left(\frac{p^2}{2m}+V(x)\right)} \frac{dxdp}{2\pi\hbar} = \\ &= \int_{x>-x_0} e^{-\beta\left(\frac{p^2}{2m}+V(x)\right)} \frac{dxdp}{2\pi\hbar} - \int_0^{V_b} \frac{da}{dE} e^{-\beta E} dE \end{aligned} \tag{4.6}$$

where in the last term $\frac{da}{dE} = \frac{\tau(E)}{2\pi\hbar}$ for $E < V_b$ is obtained from eq. (3.12b).

To consistently connect at $E \approx V_b$ the two above escape rate contributions we include the third term $\langle\Gamma\rangle_{\mathrm{tr}}$ which corresponds to the fractional phase space quantum shaded in light-red in fig. 4.2 and accounted for neither by $\langle\Gamma\rangle_{\mathrm{res}}$ nor $\langle\Gamma\rangle_{\mathrm{cont}}$. We treat $\langle\Gamma\rangle_{\mathrm{tr}}$ similarly as a single term in

$\langle\Gamma\rangle_{\mathrm{res}}$ but due to the reduced phase space area it gets a reduced statistical weight $a_{n_b} < 1$ which is the non-integer part of $a(V_b) = 18u/5\pi$. Thus,

$$\langle\Gamma\rangle_{\mathrm{tr}} = Z^{-1} a_{n_b}(u)\; e^{-\beta E_{n_b}} \Gamma_{n_b} \tag{4.7a}$$

$$Z_{\mathrm{tr}} = a_{n_b}(u)\; e^{-\beta E_{n_b}} \tag{4.7b}$$

$$a_{n_b}(u) := 18u/5\pi - \lfloor 18u/5\pi \rfloor \tag{4.7c}$$

The results for $\langle\Gamma(u)\rangle_{k_B T}$ are shown and described in fig. 4.3. We note that it has the expected behavior in both the low- and high-temperature limits with the transition happening, as expected [38], at the crossover temperature

$$k_B T_0 := \frac{\hbar\omega_0}{2\pi}, \tag{4.8}$$

To validate our model rate $\langle\Gamma(u)\rangle_{k_B T}$ also for the transition around $T \approx T_0$ we compare it in fig. 4.4 to data [30, 31] where the authors have measured escape rates of the Josephson junction from its superconducting zero-voltage state to its dissipative non-zero voltage state at different values of temperature T and bias current I. Theoretically, this corresponds to the abstract particle moving in the potential $U(\phi)$, eq. (2.10), tunneling out from the cubic potential well. The data is reported in terms of an effective temperature T_{eff}

$$k_B T_{\mathrm{eff}} := \frac{V_b}{-\ln\big(2\pi\Gamma/\omega_0\big)} \tag{4.9}$$

where the escape rate Γ is to be understood as measured and ω_0 and V_b as computed using the cubic potential, replacement rules (2.11) and experimentally determined values I_0 and C. For the data-points (red dots) in fig. 4.4 the bias current I is adjusted for each physical temperature T to always maintain $2\pi\Gamma/\omega_0 = e^{-11}$.

The model prediction in fig. 4.4 (black curve) corresponds to a level-line $\langle\Gamma/\omega_0\rangle_{k_B T} = e^{-11}/2\pi$ in the $(\, k_B T\, ;\, u\,)$ plane. With its only potential fit parameter Ω_b calculated using the replacement rules (2.11) and the experimentally determined values for I_0 and C we view the overall agreement between the model and data as very good, thus, validating our model rate $\langle\Gamma\rangle_{k_B T}$ also for temperatures around the crossover, $T \approx T_0$. The slight mismatch at higher temperatures can be explained qualitatively by the more accurate classical Klein-Kramers equation which typically predicts [37] a correction factor in eq. (4.5) that lowers the classical escape rate Γ_{cl}.

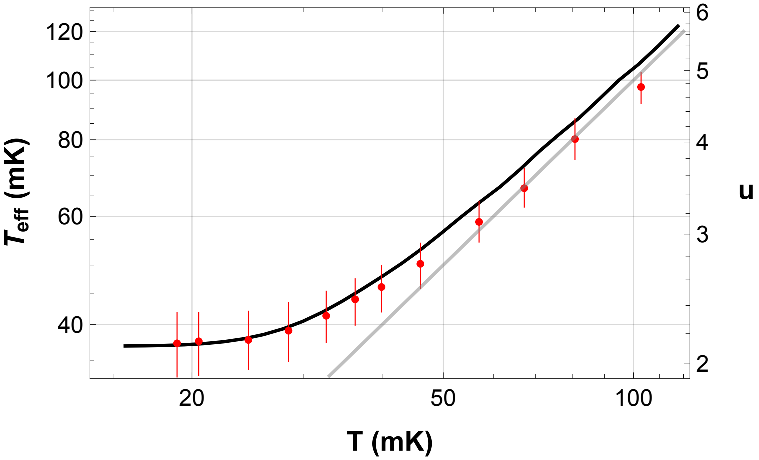

Figure 4.4: Validation of the model escape rate $\langle\Gamma\rangle_{k_BT}$ against data [30, 31] from Josephson junctions. Horizontal axis – physical temperature T, vertical axis – effective temperature $T_{\text{eff}} = -(V_b/k_B)/\ln(2\pi\Gamma/\omega_0)$. u – number of superconducting states of the junction. As the data (red dots) has been taken while satisfying the condition $\ln(2\pi\Gamma/\omega_0) = -11$ the temperature T_{eff} can also be interpreted as simply the barrier height V_b. Black curve – the corresponding prediction using the model escape rate $\langle\Gamma\rangle_{k_BT}$, grey curve, $T_{\text{eff}} = T$, – the classical prediction from $\Gamma_{\text{cl}} = \omega_0\, e^{-V_b/k_BT}/2\pi$.

4.2. Charge capture at non-zero temperature

In this section, we model electron capture experiments by taking into account non-zero temperature in the QD. This task is complicated by the fact that the confinement potential changes continuously in time so that a thermalization timescale has to compete with the decoupling time t_c. For simplicity, we only model the two extremes of this competition – for instantanous thermalization we formulate a capture probability $\langle N\rangle_{\text{fast}}$ and for infinitely slow thermalization we formulate $\langle N\rangle_{\text{slow}}$. Comparing these two models to experimental data, neither gives satisfactory quantitative agreement, nevertheless, we are still able to estimate the cubic potential energy scale $\hbar\Omega_b$. This allows further estimation of any other dimensional cubic model quantity for the experimental system which is the most significant result of the present chapter 4.

For the fast thermalization case, we simply replace in eq. (3.4) the generic escape rate Γ with the thermal escape rate $\langle\Gamma(u)\rangle_{k_BT}$ so that

$$\langle N\rangle_{\text{fast}} = \exp\Big\{-\frac{\omega_0}{\dot{u}}\int_{u_0}^{\infty}\langle\,\Gamma/\omega_0\,\rangle_{k_BT}\,du\Big\} \tag{4.10}$$

The corresponding $-(\dot{u}/\omega_0)\ln\langle N\rangle_{\text{fast}}$ as a function of u_0 can be seen in fig. 4.5b as the coloured curves.

In the slow thermalization case $\langle N\rangle_{\text{slow}}$ temperature enters only through a Boltzmann distribution over the initial conditions – either the existing discrete states n or the continuum – at $t = t_0$. The capture probabilities corresponding to each of these cases is, for the discrete states, given by eq. (3.4) with Γ replaced by Γ_n or, for the continuum, simply 0 which is reasonable for $\dot{u}/\omega_0 \ll 1$. Thus,

$$\langle N\rangle_{\text{slow}} = \big\langle e^{-\int_{t_0}^{\infty}\Gamma_n(t)dt}\big\rangle_{k_BT} = \frac{1}{Z(u_0,\beta)}\sum_{n=0}^{n_b} a_n(u_0)e^{-\beta E_n(u_0)}e^{-(\omega_0/\dot{u})\,M_n(u_0)} \tag{4.11}$$

where $Z(u_0,\beta)$ is computed using eq. (4.2b) and $a_{n<n_b} = 1$. The corresponding $-(\dot{u}/\omega_0)\ln\langle N\rangle_{\text{slow}}$ as a function of u_0 can be seen in fig. 4.5c as the coloured curves.

From the two model figures 4.5b and 4.5c one can see that irrespective from the assumed thermalization rate thermal activation – deviations from the zero-temperature ground state tunneling case given by the black dashed curves – is predicted around the same temperature $k_BT = \hbar\Omega_b/2\pi$. Thus, we define a crossover temperature in electron capture experiments

$$k_BT_{0,\,\text{capt}} := \hbar\Omega_b/2\pi \tag{4.12}$$

using which we will be able to estimate $\hbar\Omega_b$ from data by observing thermal activation in it.

The experimental data with which we compare the two models is plotted in fig. 4.5a. It has been obtained from the same QD as in chapter 3, from the one which was driven by a linear $V_S(t)$. All of the experimental capture probabilities $\langle N\rangle_{\text{exp}}$ have been measured using the same driving rate s, corresponding to $\dot{u}/\omega_0 \approx 2\cdot 10^{-4}$, but with a variable temperature starting from $T = 1.5$ K and going up to $T = 6.0$ K. The data has been plotted with $-(\dot{u}/\omega_0)\ln\langle N\rangle_{\text{exp}}$ on the vertical axis while on the horizontal axis we show the cubic model depths u_0 inferred using parameters $\tilde{\alpha}$ and V_D^c from fig. 3.8c. We observe in fig. 4.5 that neither of the models can really replicate the data on the whole range of depths u_0. The curves from $\langle N\rangle_{\text{fast}}$ are too straight and simple while $\langle N\rangle_{\text{slow}}$ displays an extra up-down oscillation at intermediate depths, not present in the data. Additionally, neither model exhibits a crossing of the different temperature lines slightly visible in data at the smallest depths. The possible physical reasons for the

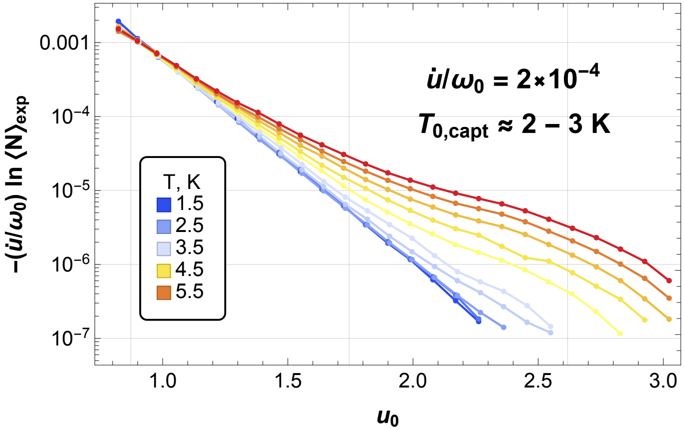

(a) Temperature-dependent capture probability data $\langle N\rangle_{\mathrm{exp}}$

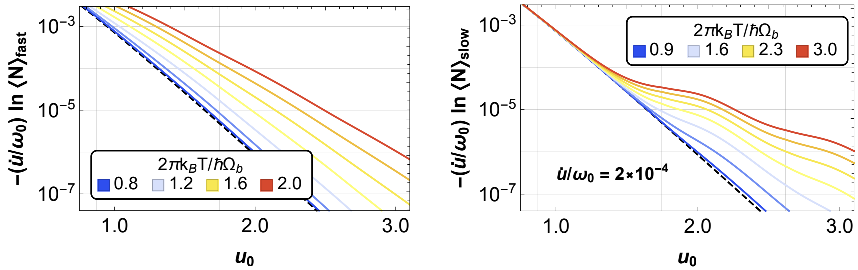

(b) Fast thermalization model $\langle N\rangle_{\mathrm{fast}}$ **(c)** Slow thermalization model $\langle N\rangle_{\mathrm{slow}}$

Figure 4.5: Experimental temperature-dependent capture probabilities $\langle N\rangle_{\mathrm{exp}}$ compared to two temperature-dependent models with fast or slow thermalization, $\langle N\rangle_{\mathrm{fast}}$ or $\langle N\rangle_{\mathrm{slow}}$. $\langle N\rangle$ given as $-(\dot{u}/\omega_0)\ln\langle N\rangle$. **(a)** Experimental data. The initial depths u_0 and the dimensionless speed $\dot{u}/\omega_0$ are obtained using results from fig. 3.8c. Thermal activation is observable at temperature $2-3\,\mathrm{K}$. **(b)** and **(c)** Coloured curves – temperature dependent results for $\langle N\rangle_{\mathrm{fast}}$ and $\langle N\rangle_{\mathrm{slow}}$, respectively. The black dashed curves – zero-temperature prediction $\int_{u_0}^{\infty}(\Gamma/\omega_0)du$ assuming tunneling only from the ground state. For both models, deviations from the ground state case start around temperature $k_B T_{0,\ \mathrm{capt}} := \hbar\Omega_b/2\pi$.

mismatch could be at least two: 1) a finite thermalization rate which could be modeled classically using the Klein-Kramers equation [37], 2) a finite temperature T_S of the source lead for which using the kinetic equation (3.1) would still be enough.

Despite not having observed a good quantitative match between

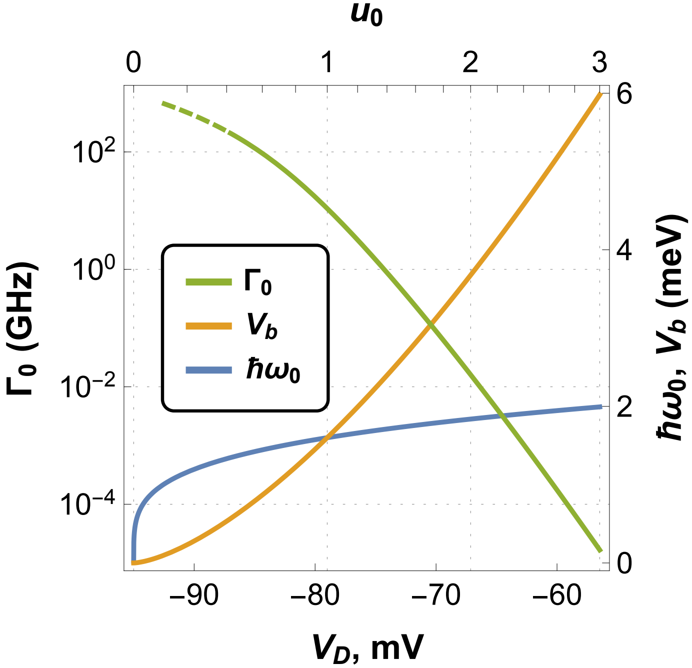

Figure 4.6: Characterization of an experimental QD in its shallow regime using its estimated cubic model energy scale $\hbar\Omega_b$, here taken to be 1.6 meV. The level-spacing $\hbar\omega_0$, barrier height V_b and ground state tunnel rate Γ_0 are known for each cubic potential depth u_0 and at the emergence of the QD from the Fermi sea at the start of backtunneling for each drain gate voltage setting V_D.

data and either of the models we can still estimate the cubic potential energy scale $\hbar\Omega_b$ using eq. (4.12). For the data we estimate the crossover temperature $T_{0,\,\mathrm{capt}}$ to be in the range $2 - 3$ K which corresponds to $\hbar\Omega_b$ in the range $1.1 - 1.6$ meV. Knowing $\hbar\Omega_b$ is actually quite significant because, whereas the results of chapter 3 allowed determining only the dimensionless quantities of depth u_0 and driving rate $\dot{u}/\omega_0$, $\hbar\Omega_b$ allows us further characterizing the experimental QD using any dimensional quantity that can be computed in the cubic model. For example, the level-spacing and barrier height are then seen from $\hbar\omega_0 = \hbar\Omega_b u^{1/5}$ and $V_b = \hbar\Omega_b u^{6/5}$ to have the same meV scale as $\hbar\Omega_b$. Their u- and V_D-dependence is depicted in fig. 4.6. The $\hbar\Omega_b \sim$ meV scale corresponds to the frequency scale $\Omega_b \sim$ THz for the oscillations of the captured electron in the shallow longitudinal direction. The scale $\Omega_b \sim$ THz also gives a rough upper limit for the cubic ground state tunnel rate Γ_0, which would be important in practice as a speed limit in many applications of tuneable barrier quantum dot devices. In fig. 4.6 we can see that Γ_0 approaches this limit in the regime where the dot is on the brink of disappearing, $u_0 \approx 0.5$, and can then further be tuned to lower values over more than 6 orders of magnitude by choosing a depth u_0 between 0.5 and 3. Finally, $\hbar\Omega_b$ also enables calculating the spatial and time-scales used in the dimensionless cubic Schrodinger equation (2.7). For the data analyzed here, the decoupling time t_c between $u = 0$ and $u = 1$ is $t_c \sim 3\,\mathrm{ns}$ and the harmonic oscillator spatial confinement scale $\sqrt{\hbar/m\Omega_b} \sim 30$ nm. These can be compared to experimentally known scales to perform consistency checks between the cubic model and experiment.

5. NON-ZERO MAGNETIC FIELD

In this chapter, we turn to the setting of a constant non-zero magnetic field perpendicular to the 2D plane for the movement of the two-dimensional electron gas. This is an important case in practice for both QD applications from sec. 1.3 – the single-electron pumps as well as electron quantum optics. In sec. 5.1, we show theoretically how the one-dimensional cubic potential model can still be used if there is at least one mechanism of electron confinement – magnetic or transverse electrostatic – that is stronger than the electrostatic cubic longitudinal confinement. We find that, essentially, the only effect of the B field is to rescale the mass of the electron which, then, implies further rescalings of all the other mass-dependent quantities. Then, in sec. 5.2 we use these rescalings to compare this model with magnetic field dependent electron pump data.

5.1. Dimensional reduction

Considering electrostatic cubic confinement $V(x)$ along the longitudinal x direction, electrostatic quadratic confinement $m\omega_y y^2/2$ along the transverse y direction and parametrizing the B field with the cyclotron frequency $\omega_c = eB/m$ we write our initial Hamiltonian in the Landau gauge as

$$\mathcal{H}_{\text{2D}} = \frac{(p_x - m\omega_c\, y)^2 + p_y^2}{2m} + \frac{m\,\omega_y^2\, y^2}{2} + V(x) \tag{5.1}$$

To show that the movement along the x direction can still, under the condition $\omega_0 \ll \max(\omega_c, \omega_y)$, be seen as determined by a 1D cubic potential we perform a unitary transformation on the Hamiltonian $\mathcal{H}_{2D} \to \widetilde{\mathcal{H}}_{2D}$

$$\widetilde{\mathcal{H}}_{2D} := e^{S}\mathcal{H}_{2D}e^{-S} \tag{5.2a}$$

$$S := \frac{i\omega_c p_x p_y}{m\hbar\Omega^2} \tag{5.2b}$$

$$\Omega^2 := \omega_y^2 + \omega_c^2 \tag{5.2c}$$

where the frequency Ω being large will enable the simplification to a one-dimensional description.

The transformed Hamiltonian is

$$\widetilde{\mathcal{H}}_{2D} = \frac{p_x^2}{2\big(1+\omega_c^2/\omega_y^2\big)m} + \frac{p_y^2}{2m} + \frac{m\Omega^2 y^2}{2} + V\Big(x + \frac{\omega_c}{m\Omega^2}p_y\Big) \tag{5.3}$$

where the variables x and y still represent the physical spatial coordinates to some extent because the transformation e^{-S} smears wave-functions $\psi(x, y)$ over a spatial scale $(\omega_c/\omega_y + \omega_y/\omega_c)^{-1}\sqrt{\hbar/m\omega_y}$. In the Hamiltonian $\widetilde{\mathcal{H}}_{2D}$ there is still interaction between variables x and y because, after expanding the cubic polynomial of the potential V, a term containing xp_y^2 and another containing x^2p_y appears. Nevertheless, if we assume now that the cubic confinement is much weaker than electrostatic transverse or magnetic confinement,

$$\omega_0^2 \ll \Omega^2 = \omega_y^2 + \omega_c^2, \tag{5.4}$$

then the dynamics for y will be dominated by a harmonic oscillator with an energy gap $\hbar\Omega$ much larger than the interaction terms. Any transitions changing the excitation number n_y along y will be canceled out by the dynamics itself on a time-scale Ω^{-1} which will be much shorter than the time-scale $\sqrt{1+(\omega_c/\omega_y)^2}\,\omega_0^{-1}$ for movement along the x direction. Thus, movement in each subspace with a definite n_y can be described separately using its own Hamiltonian $\mathbb{P}_{y,n}\widetilde{\mathcal{H}}_{2D}\mathbb{P}_{y,n}$ where the $\mathbb{P}_{y,n}$'s project onto the subspaces with fixed n_y. In principle, the corresponding Hamiltonians for movement along x depend on n_y, nevertheless, using condition (5.4) and considering only the lowest n_y's all of them are approximated by the same one-dimensional magnetic field dependent cubic potential Hamiltonian

$$\mathcal{H}(B) = \frac{p_x^2}{2(1+\omega_c^2/\omega_y^2)m} + \frac{bx^3}{3} - Fx + V_b/2, \qquad \omega_c = eB/m \tag{5.5}$$

We see that the obtained Hamiltonian is almost identical to the initial cubic model Hamiltonian, eq. (2.2), with the only difference – the factor $(1+\omega_c^2/\omega_y^2)$ multiplying the mass m of the electron. Thus, it is like the electron gets more massive due to magnetic field. From this, we define a B-field rescaled mass $m(B)$

$$m(B) := m\,\zeta^2(B) \tag{5.6a}$$
$$\zeta^2(B) := 1 + \omega_c^2(B)/\omega_y^2 = 1 + B^2/B_0^2 \tag{5.6b}$$
$$B_0 := m\omega_y/e \tag{5.6c}$$

where $\zeta(B) \geq 1$ is the scaling factor and B_0 – the crossover field around and above which magnetic field effects should start being observable. As B_0 depends on ω_y this could be used for determining ω_y in an experiment.

In the cubic model, several important quantities depend on mass m so also these will get rescaled by the B field:

$$\omega_0(B) = \frac{\omega_0(0)}{\zeta(B)} \tag{5.7a}$$
$$u(B) = u(0)\zeta(B) \tag{5.7b}$$
$$\left.\frac{\dot{u}}{\omega_0}\right|_B = \left.\frac{\dot{u}}{\omega_0}\right|_{B=0}\zeta^2(B) \tag{5.7c}$$
$$\Omega_b(B) = \frac{\Omega_b(0)}{\zeta^{6/5}(B)} \tag{5.7d}$$

In the next section 5.2, we will combine eq.'s (5.7b) and (5.7c) with already developed ideas and data-analysis techniques from chapter 3 to model the B-field dependence in electron pump data. More qualitatively, one can also see that eq. (5.7c) predicts that an increasing B field should also increase non-adiabatic excitation effects which fits well with eq. (5.7d) correspondingly predicting a decrease in the speed of a QD-based device (see discussion after eq. (2.9)).

5.2. Comparison to experiment

In this section, we demonstrate how the magnetic field dependent model of cubic confinement presented in the previous section 5.1 can be used to analyze and interpret experimental data. For this, we use data [39] from single electron current pumps where a non-zero magnetic field is observed to: 1) sharpen the $0 \to ef$ current step and 2) enable non-adiabatic excitations in the QD. Despite a good looking fit we do not observe full consistency between the theory and experiment. We discuss the possible physical reasons which may be causing this which, then, leads us to the main conclusions of the present chapter 5.

To model B field dependent electron capture or the closely related electron pumping experiments with the cubic model we simply reuse its eq. (3.4) applied for the ground state, $\Gamma = \Gamma_0$, only now we use the B field dependent depth and speed, eq.'s (5.7b) and (5.7c):

$$\langle N\rangle = \exp\Big\{ - \Big(\frac{\dot{u}}{\omega_0}\Big|_{B=0} \zeta^2(B)\Big)^{-1} M_0\Big(\zeta(B)\,[\tilde{\alpha}(V_D - V_D^c)]^{5/4}\Big)\Big\} \tag{5.8}$$

This assumes that neither the electrostatic confinement potential $V(t,x)$ nor the Fermi level ϵ_F of the source are influenced by the B field. Additionally, we have used here $u_0(B=0, V_D) = [\tilde{\alpha}(V_D - V_D^C)]^{5/4}$, eq. (3.15), which can be seen as describing the B field independent shape of the potential.

The resulting B field dependent capture probabilities predicted by eq. (5.8) are shown in fig. 5.1a as functions of the dimensionless drain gate voltage $\tilde{\alpha}(V_D - V_D^c)$. Two effects are observable while increasing the $B = m\omega_c/e$ field: 1) a shift of the capture probability step $\langle N\rangle = 0 \to 1$ towards more negative voltages and 2) a sharpening of this step. For a qualitative comparison of the sharpening effect to data we give fig. 5.1b. In eq. (5.8), the sharpening happens because the increase of the effective mass $m(B)$ makes, at any voltage V_D, the number of initial confined states u_0 larger so that the function $u_0(V_D) = \zeta(B)\,[\tilde{\alpha}(V_D - V_D^c)]^{5/4}$ becomes steeper in $M_0(u_0(V_D))$.

For a quantitative comparison between the model and experiment we use data from [39]. There, a QD was operated as a single electron pump at a range of pump frequencies f which we assume to be proportional to $\dot{u}/\omega_0|_{B=0}$ from the cubic model. The measured quantity is the current

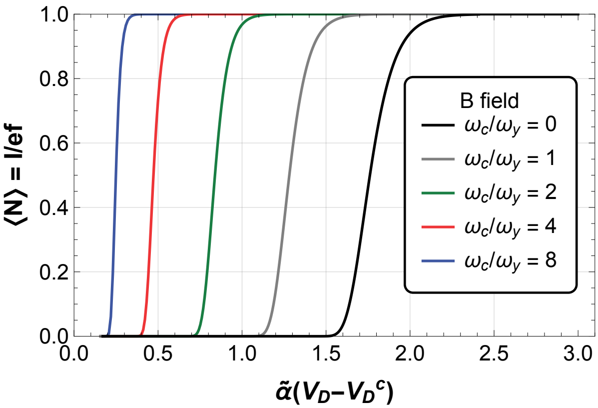

(a) Cubic potential model, $\frac{\dot{u}}{\omega_0}\big|_{B=0} = 10^{-6}$

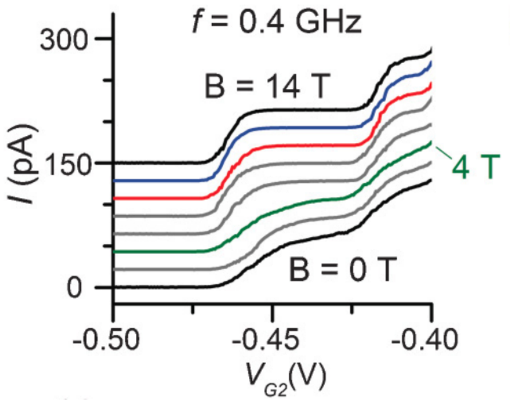

(b) Experimental data [16].

Figure 5.1: $B = m\omega_c/e$ field dependent capture probability step $\langle N \rangle = I/ef = 0 \to 1$ sharpening in **(a)** the cubic model and **(b)** experimental data from [16]. Different magnetic field values are encoded by colour, differently for the model and data. For data, each consecutive experimental curve has an increased magnetic field by 2 T and the curves have been shifted vertically and horizontally for clarity of the current steps.

I flowing through the QD and its relation to the capture probability is $\langle N\rangle = I/ef$. We will consider from [39] capture probability step widths of figure 2(a) there and non-adiabatic excitation lines of figure 2(c) there. The data in the experimental figure 2(a) was obtained at a pump frequency $f = 100\,\mathrm{MHz}$ and the first current step $I/ef = \langle N\rangle = 0 \to 1$ there is interpreted as coming from single electron escape from the QD ground state. The data in the experimental figure 2(c), also plotted in fig. 5.2d here, was obtained at an increased pump frequency $f = 1\,\mathrm{GHz}$. The data is presented after aligning all ground state current steps at the bottom of the plot. This is done to focus on the 3 paler current steps which are interpreted as being due to non-adiabatic excitation to higher states, possible because of the increased driving rate of the QD. These extra current steps have, essentially, the same interpretation as in the ground state case – as a transition from no capture to complete capture – only now the electron tunnels out from an excited state $n > 0$.

To model this data we first need for the ground and excited states n their dimensionless voltage-positions $\mathrm{v}_n(B, \dot{u}/\omega_0|_{B=0})$ of their current steps. More precisely, v_n gives in fig. 5.1a the horizontal locations $\tilde{\alpha}(V_D - V_D^c)$ where $\langle N\rangle_n = 1/2$ hold, where $\langle N\rangle_n$ is given by eq. (5.8) and used also for the excited states, $M_0 \to M_n$. The voltages v_n can be written as

$$\mathrm{v}_n\Big(B, \frac{\dot{u}}{\omega_0}\Big|_{B=0}\Big) = \Big\{\frac{1}{\zeta(B)} u_{0,\ln M_n}\Big(\ln[\zeta^2(B)] + \ln\frac{\dot{u}}{\omega_0}\Big|_{B=0} + \ln(\ln 2)\Big)\Big\}^{4/5} \tag{5.9}$$

$$u_0 =: u_{0,\ln M_n}\big(\ln M_n(u_0)\big) \tag{5.10}$$

where it was necessary for us to define the inverse functions $u_{0,\ln M_n}(\ldots)$ for the relations $u_0 \to \ln M_n(u_0)$.

Next, we want to quantify the current step widths in the 100 MHz data. For this, we take the decay cascade model [32] Ansatz $I(V_D)/ef = \langle N\rangle = \exp\big\{-\exp\big\{-\alpha_{\mathrm{dc}}V_D + \delta\big\}\big\}$ from which we interpret

$$\alpha_{\mathrm{dc}}^{-1} = \Big(-\frac{d}{dV_D}\ln[-\ln\langle N\rangle]\Big)^{-1} \tag{5.11}$$

as the needed current step width. From fitting the decay cascade Ansatz to data we obtained experimental B field dependent step widths $\alpha_{\mathrm{dc,\,exp}}^{-1}(B)$ which we show as the black dots in fig. 5.2b up to the field value $B = 4\,\mathrm{T}$. To obtain the corresponding model prediction we compute $-\frac{\partial}{\partial V_D}\ln\big[-\ln\langle N\rangle\big]$ for eq. (5.8) and evaluate the result at $\tilde{\alpha}(V_D - V_D^c) = \mathrm{v}_0$.

From this, we can write down the predictions for both datasets as

$$\alpha_{\mathrm{dc}}^{-1}(B) = \Big(\frac{5}{4}\tilde{\alpha}\zeta \mathrm{v}_0^{1/4}\frac{\Gamma_0/\omega_0}{M_0}\Big|_{\mathrm{v}_0^{5/4}\zeta}\Big)^{-1} \tag{5.12}$$

$$\Delta V_{D,n}(B) = \tilde{\alpha}^{-1}(\mathrm{v}_n - \mathrm{v}_0) \tag{5.13}$$

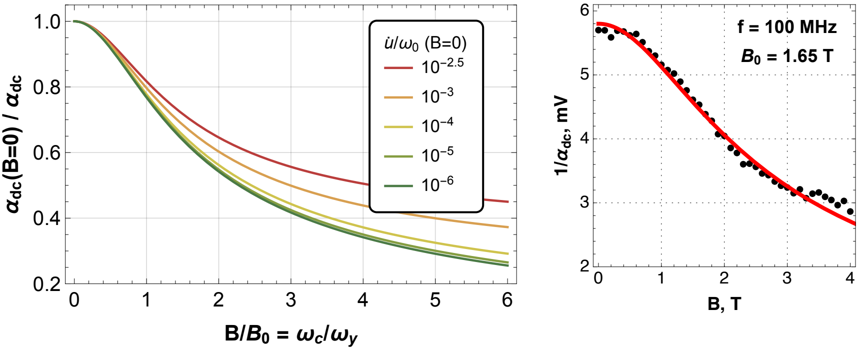

(a) Predicted current step widths α_{dc}^{-1} in B field

(b) Fit of (a) to data

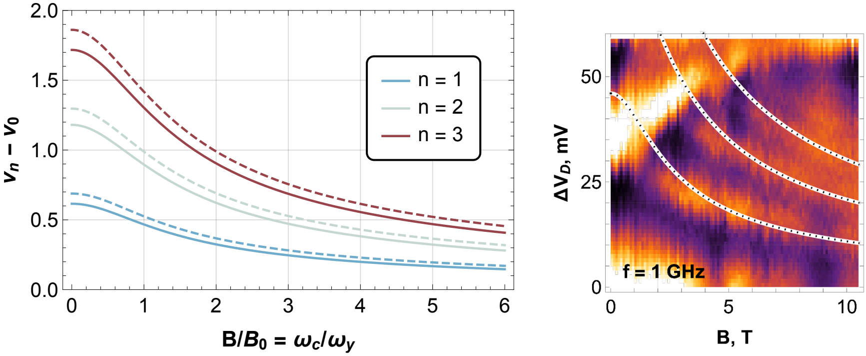

(c) Predicted distances between excited and ground state current steps.

(d) Fit of (c) to data

Figure 5.2: (a) and (c) – cubic model predictions for the magnetic field B dependence in single electron pump data, (b) and (d) – comparisson to data [39]. **(a)** Predicted ground state current step $I/ef = 0 \to 1$ widths $\alpha_{\text{dc}}^{-1}(B)$. Dependence on $\frac{\dot{u}}{\omega_0}\big|_{B=0}$ at smaller driving speeds $\frac{\dot{u}}{\omega_0}\big|_{B=0}$ is very weak. **(b)** Model curves in (a) fitted to data. The experimental points $\alpha_{\text{dc, exp}}^{-1}(B)$ have been obtained by doing a decay-cascade fit to pump current data $I(V_D)$. **(c)** Predicted distances along voltage V_D between the excited state n current steps and the ground state current step. For solid lines $\frac{\dot{u}}{\omega_0}\big|_{B=0} = 10^{-20}$ while for dashed lines $\frac{\dot{u}}{\omega_0}\big|_{B=0} = 10^{-3}$. **(d)** Model curves in (c) fitted to data. Lighter shades in data correspond to larger derivative $\partial I/\partial V_D$ to show the positions of the ground and excited state current steps.

where $\alpha_{\text{dc}}^{-1}(B)$, shown in fig. 5.2a, give the current step widths for the 100 MHz data and $\Delta V_{D,n}(B)$, shown in fig. 5.2c, give the distances along V_D between the excited state n and ground state current steps in the 1 GHz data. Both types of B-field dependent curves depend on 3 parameters – the scale B_0 for B field, a scale $\tilde{\alpha}^{-1}$ for voltages V_D and the zero-field driving speed $\dot{u}/\omega_0|_{B=0}$. The critical voltage V_D^c has dropped out. A simultaneous fit of $\alpha_{\text{dc}}^{-1}(B)$ and $\Delta V_{D,n}(B)$ to both datasets is shown in fig.'s 5.2b and 5.2d where the parameters $B_0 = 1.65\,\text{T}$ and $\frac{\dot{u}}{\omega_0}\Big|_{B=0}^{1\,\text{GHz}} = 10^{-17}$ and $\tilde{\alpha}^{-1} = 74\,\text{mV}$ have been used. We note that with this at $B = 0$ the depths u_0 are 5.6 and higher and comment on the large uncertainty in driving speed – $\frac{\dot{u}}{\omega_0}\Big|_{B=0}^{1\,\text{GHz}}$ between 10^{-23} and 10^{-13} – which is due to the extremely weak dependence on $\dot{u}/\omega_0|_{B=0}$ of the model curves, especially at lower speeds $\dot{u}/\omega_0|_{B=0}$.

Although the fits in fig. 5.2b and 5.2d between theory and data look convincing, they are, unfortunately, not fully consistent with the experiment. We try to show this as follows: as we have tried to achieve an equally good fit for all B-field values, also small ones, $B \to 0$, we have, effectively, assumed that the condition $\omega_0 \ll \Omega$ is satisfied already due to $\omega_0 \ll \omega_y$ (electrostatic potential elongated along x). Calculating $\omega_y = 4.3\,\text{THz}$ from eq. (5.6c) we can write $\Omega_b \sim \omega_0 \ll \omega_y = 4.3\,\text{THz}$ and then compute a lower bound for the decoupling time t_c from eq. (2.9)

$$t_c = \frac{5}{4}\frac{\Omega_b^{-1}}{\dot{u}/\omega_0} \gg \frac{5/4}{10^{-13}\cdot 4.3\,\text{THz}} \sim 1\,\text{sec} \tag{5.14}$$

This is a clear contradiction to the experimentally known driving frequency $f = 1\,\text{GHz}$ because all characteristic time scales of the electron capture or pumping process should be below the corresponding driving period of 1 ns.

In the following, we discuss two possible reasons for the inconsistency which then leads us to the main conclusions of the present chapter 5. The first possible reason might be that the implicit assumption[1] $\Omega_b \ll \omega_y$ of the performed fit is not adequate for this sample and, rather, $\Omega_b \sim \omega_y$ is more accurate, similarly to what was suggested in the original paper [39]. In this case, a fit of the model curves would still make sense if high enough magnetic fields can be reached so that $\Omega_b \ll \omega_c$ holds. Then, one should give more attention and weight in the fits to the high field data because there the model would be more justified. We could speculate that the excitation lines in fig. 5.2d fit so well because for them $\Omega_b \ll \omega_c$ is already satisfied while fig. 5.2b is the one causing problems because $\Omega_b \ll \Omega$ does not yet hold there. Nevertheless, if we assume that magnetic field effects, still, start to appear around $\omega_c \sim \omega_y$ also for the case $\Omega_b \sim \omega_y$ then we

---

[1] We use in this discussion Ω_b, instead of ω_0, because, during electron capture, Ω_b is time-independent and $\omega_0/\Omega_b = u^{1/5} \sim 1$.

still have inferred the order of magnitude for B_0 and ω_y correctly. Then, for this experiment, $\Omega_b \sim \omega_y \sim$ THz which is the same scale for Ω_b that we obtained in chapter 3 from another experiment in another GaAs/AlGaAs device.

The second possible reason for the inconsistency could be that the one-dimensional cubic potential approximation holds robustly only for the ground state. For the excited states which have a higher energy the approximation that the potential energy is a sum of two one-dimensional potential energies in two transverse directions does not hold so well and this influences both the quantized energies as well as the tunnel rates. If this were true then one way of modelling this "non-separation of variables" would be to consider all the other cubic expansion terms in 2 dimensions – the additional terms x^2y, xy^2 and y^3. While this would seem a reasonable direction to think about this would introduce many extra parameters – so one would, again, have to be careful about this and somehow reduce their number.

To conclude, we have demonstrated in this chapter how the simple one-dimensional cubic potential model can be used to model and analyze tuneable barrier quantum dot based devices and data from them in non-zero magnetic field assuming that cubic confinement in the longitudinal direction is weaker than quadratic confinement in the transverse direction, $\Omega_b \ll \omega_y$, or weaker than magnetic confinement, $\Omega_b \ll \omega_c$, or both simultaneously. The inconsistency between theory and experiment implied by the fits in fig. 5.2 suggests expanding the range of conditions which are modeled. In general, the explicit modeling of the transverse direction and its influence on energies and tunnel rates seems necessary. From the two above possibilities how the transverse spatial direction could start influencing the escape dynamics the considerably simpler case to consider would be to allow for a roughly isotropic electrostatic confinement, $\Omega_b \sim \omega_y$, because the alternative – breakdown of separation of longitudinal / transverse variables at zero magnetic field – would come, initially, with several more extra parameters in the potential energy. Moreover, even if the here considered electrostatic confinement regime with $\Omega_b \ll \omega_y$ would have been verified experimentally the case $\Omega_b \sim \omega_y$ would need future attention anyway. Because if one would really take Ω_b seriously as the speed of a device and would like to increase Ω_b this kind of optimization would then lead from the initial regime $\Omega_b \ll \omega_y$ to $\Omega_b \sim \omega_y$ anyway.

6. CONCLUSION

6.1. Conclusions and discussion

In this doctoral thesis:

1. the potential usefulness of the simple one-dimensional cubic potential assumption, $V(t,x) = b\,x^3/3 - \dot{F}t\,x$, has been demonstrated in modeling the regime of shallow confinement for **maximally fast operation** of tuneable-quantum-dot-based devices. It can be expected that this assumption describes a **universal regime of operation** available to a broad range of experimental realizations.

2. it has been explained how to **fully relate** an experimental quantum dot in the shallow regime **to the cubic model** – how to determine quantities like the number of confined states, barrier height, tunnel rates, etc. and their gate voltage dependence.

3. the theoretical frequency scale $\Omega_b = \left(6b^2\hbar/m^3\right)^{1/5}$ has been identified as the frequency scale which **sets limits** simultaneously for the operation speed as well as robustness against thermal excitations of tuneable-quantum-dot-based devices, e.g., the most accurate electron pumps or single electron sources.

For a more detailed discussion of conclusions nr. 2. and 3. see the last paragraphs of sec. 4.2 and 2.2, respectively. For the remainder of this section we expand on the most general conclusion nr. 1. We believe that the simple one-dimensional cubic model explored in this work could be potentially of great use in the further development of tuneable quantum dot based devices. In particular, it should be useful for characterizing and optimizing devices which operate in the shallow regime where we expect our model to be universally valid across a broad range of experimental realizations. As the tunneling rates approach their maximum possible values in this regime we hope that our model will be of great aid in pushing up the limits of maximum operation speeds. For this, we have identified the particular frequency scale $\Omega_b = \left(6b^2\hbar/m^3\right)^{1/5}$ as the crucial device parameter which should be optimized towards higher values for a faster operation. We see two possible ways in trying to achieve this: 1) the cubic potential coefficient b which gives the steepness of the potential at the emergence of confinement could be increased by optimizing the device geometry and 2) to decrease the electron effective mass m a change of the material of the device would be necessary.

One technological area where such an increased operation speed would be desirable is electrical current metrology. Currently, quantum dot based single electron pumps can be used to generate currents in the 100 fA − 100 pA range with precision $10^{-7} - 10^{-6}$. At increased currents in the 1 μA − 1 mA range an alternative method of generating current – the Josephson voltage standard combined with the quantum Hall resistance [40] – can be used with precision $\sim 10^{-8}$. However, in between these ranges, at 100 pA − 1 μA, the currently available precision is substantially lower and might be subject for improvement. One way of tackling this problem would be to try to close this gap from below by increasing the output current $I = nef$ of single electron pumps. One way to do that would be to increase the pump frequency f, however, not to lose precision one would have to make sure that the dynamics of the transported electron is able to follow the rapid changes in its environment. This would be ensured by a high enough Ω_b and, correspondingly, low enough $\dot{u}/\omega_0$ of the capture process.

Another potential application area for the results of this work could be the single electron quantum optics experiments described in sec. 1.3. The methods developed here for characterizing shallow quantum dots could be applied to the single electron sources there to better understand the initial wave packets supplied to the experiment. This may enable tuning the initial state of the electrons in a more controlled way, for example, to increase their robustness against decoherence or to compactify the corresponding distributions in phase space closer to the Heisenberg limit. Moreover, in this context, a QD with an increased Ω_b might eventually lead to sensing interferometers with an increased temporal resolution or quantum computers performing computations at an increased rate.

6.2. Open questions

We now briefly discuss the further questions raised by this work and the possible future research directions.

The first and most significant future question is about the universality of the one-dimensional cubic model – how broad is the range of real devices that can actually be described by it? After this, the next significant question would be how to increase the frequency scale Ω_b limiting the speed of the corresponding devices. An answer to the first question – about universality – could be very valuable information because it could, potentially, significantly simplify further research – because a single model would describe many devices and, additionally, enable their direct comparisons. Moreover, knowing the ”boundaries of universality” would inform further research on what is the largest set of devices on which optimization towards specific properties – like larger Ω_b – can be done in the same way, as described by the cubic model. Finally, universality in device operation is also a desired property for the metrological application of electron pumps [4]. For further experimental and theoretical methodology details on studying universality see in the main work the corresponding section to this one and for a discussion about increasing Ω_b see the preceding section 6.1 here.

Other alternative future research directions could be:

- applying the cubic model to the case of two electrons confined in the QD to compute the escape rates for the second electron. This might allow predicting an important characteristic of the output currents $I(V_D)$ of QD-based electron pumps – the position of the second current step $I(V_D)/ef = 1 \to 2$ which together with the first current step largely determine the precision of the output current $I = ef$ on the first plateau of the pump,

- considering the two-electron problem further, another future research direction would study the possible creation of two-electron bound states which become possible at strong magnetic fields [41] and which might be created during the emission of electrons from a tuneable barrier QD. For the electron pump application this might be an error mechanism giving rise to deviations of the pump current from the quantized values $I = nef$ and understanding this process could help minimize this kind of systematic error. On the other hand, in electron quantum optics these states might be an interesting way to generate two-electron entanglement or might even provide a useful basis for doing quantum computations.

- solving a time-dependent Schrodinger equation to obtain the wave-packet emitted from a gradually opened cubic QD into an electron quantum optics edge channel. This, combined with the shallow QD characterization methods discussed at the end of sec. 4.2, could lead future electron quantum optics experiments in choosing better emission protocols to obtain initial wave-packets with the desired properties which maximize the intended effects and experimental outcomes,

- solving the time-dependent Schrodinger equation for the capture problem would allow determining more precisely at which large enough QD driving speeds $\dot{u}/\omega_0$ non-adiabatic excitations of the electron start playing a role and the simple ground-state-tunneling approximation used in this work breaks down. For the metrological electron pump application, it could be expected that above some certain speed $\dot{u}/\omega_0$ non-adiabatic excitations become strong enough to decrease the precision of the electron pump output current.

ADDITIONAL INFORMATION

Author contribution

In this doctoral thesis, if not stated otherwise, all the scientific results have been obtained by the degree candidate Austris Akmentinsh (University of Latvia), his thesis supervisor Vyacheslavs Kashcheyevs (University of Latvia) and their colleague Niels Ubbelohde (Physikalisch-Technische Bundesanstalt (PTB), Braunschweig, Germany). Most of the technical theory work presented in this thesis – calculations, plots and fits – was done by Austris Akmentinsh. On a broader scale, the theory research was lead by Vyacheslavs Kashcheyevs to have a larger scientific impact. The experimental work that supplied the data that was analyzed was done by Niels Ubbelohde and his colleagues. The initial idea to use the one-dimensional cubic potential to describe shallow QDs was suggested by Peter G. Silvestrov (Technical University of Braunschweig, Germany).

To give a more precise idea for the author contribution in this doctoral thesis we list here the sections and main steps of this work which are, in the most part, due to the degree candidate:

- Analysis of the dimensionless time-dependent Hamiltonian *(sec. 2.2)*
- Scaling relation of the capture probability *(sec. 3.1)*
- Idea of a master curve following from the scaling relation *(sec. 3.2)*
- The introduction to the notion of resonances *(see the main work)*
- Implementing the complex scaling method for the cubic potential well *(sec. 3.3)*
- Idea to use the fractional phase space quantum to connect the discrete and continuous contributions to the thermal escape rate *(sec. 4.1)*
- Idea how the experimental voltage map (V_S, V_D) can be filled with the right values for depth u *(see the main work)*
- The detailed analysis of the decoupling of the transformed variables x and y in magnetic field *(sec. 5.1)*
- The fitting procedure of the B field theory to data *(sec. 5.2)*
- Observation of the contradiction in the B field fits *(sec. 5.2)*

List of publications

1. A. Akmentinsh, N. Ubbelohde, V. Kashcheyevs, “Modeling shallow confinement in tunable quantum dots”. In: *Physical Review B - Condensed Matter and Materials Physics.* As of 16.01.2025 accepted for publication. arXiv preprint: *arXiv:2408.04565*
2. A. Akmentinsh, D. Reifert, T. Weimann, K. Pierz, V. Kashcheyevs, N. Ubbelohde, “Universal scaling of adiabatic tunneling out of a shallow confinement potential”, submitted to *Physical Review Applied*, arXiv preprint: *arXiv:2301.11295*

Conferences and seminars

1. *American Physical Society (APS) March Meeting 2024*, 03.03.2024-08.03.2024, Minneapolis, USA. Two presentations, oral as well as poster, with the same name ”Modelling shallow confinement in tuneable quantum dots as a 1D cubic potential”. (Abstracts available in the epitome of the conference)
2. *82nd International Scientific Conference of the University of Latvia*, section *Quantum Sensors and Devices*, 08.02.2024, Riga, Latvia. Oral presentation ”Characterization of shallow quantum dots using the 1D cubic potential model”.
3. *722. WE-Heraeus-Seminar / Hybrid Solid State Quantum Circuits, Sensors, and Metrology*, 13.12.2021-16.12.2021, virtual format during the Covid-19 pandemic. Poster presentation ”Charging of a shallow quantum dot”. (Abstract available in the abstract booklet of the conference)
4. *78th International Scientific Conference of the University of Latvia*, special session *Physical aspects of quantum advantage for information and measurement technologies*, 29.01.2020, Riga, Latvia. Oral presentation ”Single-electron capture in a dynamic quantum dot”.

Research projects

1. Project **Latvian Quantum Initiative** (ST, FMOF) contr. Nr. 2.3.1.1.i.0/1/22/I/CFLA/001, University of Latvia reg. Nr. ESS2023/454 member as a research assistant. Project duration: 01.02.2023. - not yet finished. Financing: European Union.
2. Project **Enabling science for single-electron quantum technologies**, contr. Nr. lzp-2021/1-0232, University of Latvia reg. Nr. LZP2021/105 member as a research assistant. Project duration: 01.02.2022. – 31.12.2024. Financing: Latvian Council of Science.

3. Project **Quantum optics technology realization in nanoelectronic devices II *(Kvantu optikas tehnoloģiju realizācija nanoelektroniskajās ierīcēs II)***, University of Latvia reg. Nr. ZD2016/AZ101 member as a research assistant. Project duration: 01.01.2023. – 30.06.2023. Financing: *(in Latvian)* bāzes finansējums.

4. Project **Quantum optics technology realization in nanoelectronic devices *(Kvantu optikas tehnoloģiju realizācija nanoelektroniskajās ierīcēs)***, University of Latvia reg. Nr. AAP2016/B031 member as a research assistant. Project duration: 01.09.2020. – 31.12.2022. Financing: *(in Latvian)* snieguma finansējums.

5. Project **Physical aspects of quantum advantage for information and measurement technologies**, contr. Nr. lzp-2018/1-0173, University of Latvia reg. Nr. LZP2018/3 member as a research assistant. Project duration: 01.10.2019. – 30.09.2021. Financing: Latvian Council of Science.

6. Project **Single-electron quantum optics for quantum-enhanced measurements (SEQUOIA)**, contr. Nr. 17FUN04 SEQUIA, University of Latvia reg. Nr. ZD2018/20612 member as a research assistant. Project duration: 01.10.2019. – 31.01.2022. Financing: European Union.

Prior education

1. Master of Science in Theoretical and Mathematical Physics, Ludwig Maximilian University of Munich, 01.10.2015-01.03.2019, Munich, Germany

2. Bachelor of Science in Physics, University of Latvia, 01.09.2012-03.07.2015, Riga, Latvia

REFERENCES

[1] Feynman R. P. "There's Plenty of Room at the Bottom". In: *Engineering and Science, Caltech* 23 (1960), pp. 22–36.

[2] The Nobel Committee for Chemistry. *Quantum dots – seeds of nanoscience, Scientific Background to the Nobel Prize in Chemistry 2023*. 2023. URL: `https://www.nobelprize.org/uploads/2023/10/advanced-chemistryprize2023-3.pdf` (visited on 05/25/2024).

[3] Bernd Kaestner and Vyacheslavs Kashcheyevs. "Non-adiabatic quantized charge pumping with tunable-barrier quantum dots: a review of current progress". In: *Reports on Progress in Physics* 78 (2015). DOI: `10.1088/0034-4885/78/10/103901`. URL: `http://arxiv.org/abs/1412.7150%20http://dx.doi.org/10.1088/0034-4885/78/10/103901`.

[4] Stephen P Giblin et al. "Evidence for universality of tunable-barrier electron pumps". In: *Metrologia* 56.4 (2019), p. 044004.

[5] C.W.J. Beenakker and Henk van Houten. "Quantum transport in semiconductor nanostructures". In: *Solid state physics*. Vol. 44. Elsevier, 1991.

[6] T. Gerster et al. "Robust formation of quantum dots in GaAs/AlGaAs heterostructures for single-electron metrology". In: *Metrologia* 56.1 (Feb. 2019). ISSN: 16817575. DOI: `10.1088/1681-7575/aaf4aa`.

[7] Gento Yamahata, Nathan Johnson, and Akira Fujiwara. "Understanding the mechanism of tunable-barrier single-electron pumping: Mechanism crossover and optimal accuracy". In: *Physical Review B* 103.24 (June 2021). ISSN: 24699969. DOI: `10.1103/PhysRevB.103.245306`.

[8] Frank Hohls et al. "Controlling the error mechanism in a tunable-barrier nonadiabatic charge pump by dynamic gate compensation". In: *Physical Review B* 105.20 (May 2022). ISSN: 24699969. DOI: `10.1103/PhysRevB.105.205425`.

[9] M. Veldhorst et al. "An addressable quantum dot qubit with fault-tolerant control-fidelity". In: *Nature nanotechnology* 9.12 (2014), pp. 981–985.

[10] D.M. Zajac et al. "Scalable gate architecture for a one-dimensional array of semiconductor spin qubits". In: *Physical Review Applied* 6.5 (2016), p. 054013.

[11] Takafumi Fujita et al. "Coherent shuttle of electron-spin states". In: *npj Quantum Information* 3.1 (2017), p. 22.

[12] Friederike Stein et al. "Validation of a quantized-current source with 0.2 ppm uncertainty". In: *Applied Physics Letters* (June 2015). DOI: 10.1063/1.4930142.

[13] B. Kaestner et al. "Single-parameter nonadiabatic quantized charge pumping". In: *Physical Review B* 77.15 (Apr. 2008). ISSN: 10980121. DOI: 10.1103/PhysRevB.77.153301.

[14] Mark David Blumenthal et al. "Gigahertz quantized charge pumping". In: *Nature Physics* 3.5 (2007), pp. 343–347.

[15] Akira Fujiwara, Katsuhiko Nishiguchi, and Yukinori Ono. "Nanoampere charge pump by single-electron ratchet using silicon nanowire metal-oxide-semiconductor field-effect transistor". In: *Applied Physics Letters* 92.4 (2008).

[16] J. D. Fletcher et al. "Stabilization of single-electron pumps by high magnetic fields". In: *Physical Review B - Condensed Matter and Materials Physics* 86.15 (Oct. 2012). ISSN: 10980121. DOI: 10.1103/PhysRevB.86.155311.

[17] B Kaestner et al. "Single-parameter quantized charge pumping in high magnetic fields". In: *Applied Physics Letters* 94.1 (2009).

[18] SJ Wright et al. "Enhanced current quantization in high-frequency electron pumps in a perpendicular magnetic field". In: *Physical Review B—Condensed Matter and Materials Physics* 78.23 (2008), p. 233311.

[19] SP Giblin et al. "Towards a quantum representation of the ampere using single electron pumps". In: *Nature communications* 3.1 (2012), p. 930.

[20] Gento Yamahata et al. "Gigahertz single-electron pumping in silicon with an accuracy better than 9.2 parts in 107". In: *Applied Physics Letters* 109.1 (2016).

[21] R Zhao et al. "Thermal-error regime in high-accuracy gigahertz single-electron pumping". In: *Physical Review Applied* 8.4 (2017), p. 044021.

[22] Lukas Fricke et al. "Self-referenced single-electron quantized current source". In: *Physical Review Letters* 112.22 (2014), p. 226803.

[23] SP Giblin et al. "High-resolution error detection in the capture process of a single-electron pump". In: *Applied Physics Letters* 108.2 (2016).

[24] Ye-Hwan Ahn, Changki Hong, Young-Seok Ghee, et al. “Upper frequency limit depending on potential shape in a QD-based single electron pump”. In: *JOURNAL OF APPLIED PHYSICS* 122 (2017), p. 194502.

[25] Lars Freise et al. “Trapping and counting ballistic nonequilibrium electrons”. In: *Physical Review Letters* 124.12 (2020), p. 127701.

[26] J. D. Fletcher et al. “Continuous-Variable Tomography of Solitary Electrons”. In: *Nature communications* 10.1 (Jan. 2019). DOI: `10.1038/s41467-019-13222-1`. URL: `http://arxiv.org/abs/1901.10985%20http://dx.doi.org/10.1038/s41467-019-13222-1`.

[27] Elina Locane, Piet W Brouwer, and Vyacheslavs Kashcheyevs. “Time-energy filtering of single electrons in ballistic waveguides”. In: *New Journal of Physics* 21.9 (2019), p. 093042.

[28] P. Krantz et al. “A quantum engineer’s guide to superconducting qubits”. In: *Applied Physics Reviews* 6.2 (June 2019). ISSN: 1931-9401. DOI: `10.1063/1.5089550`.

[29] Michel H Devoret et al. “Quantum fluctuations in electrical circuits”. In: *Les Houches, Session LXIII* 7.8 (1995), pp. 133–135.

[30] Michel H. Devoret, John M. Martinis, and John Clarke. “Measurements of Macroscopic Quantum Tunneling out of the Zero-Voltage State of a Current-Biased Josephson Junction”. In: *Physical Review Letters* 55.18 (Oct. 1985), pp. 1908–1911. ISSN: 0031-9007. DOI: `10.1103/PhysRevLett.55.1908`.

[31] John M. Martinis, Michel H. Devoret, and John Clarke. “Experimental tests for the quantum behavior of a macroscopic degree of freedom: The phase difference across a Josephson junction”. In: *Physical Review B* 35.10 (Apr. 1987), pp. 4682–4698. ISSN: 0163-1829. DOI: `10.1103/PhysRevB.35.4682`.

[32] Vyacheslavs Kashcheyevs and Bernd Kaestner. “Universal decay cascade model for dynamic quantum dot initialization”. In: *Physical Review Letters* 104.18 (May 2010). ISSN: 00319007. DOI: `10.1103/PhysRevLett.104.186805`.

[33] Lukas Fricke et al. “Counting statistics for electron capture in a dynamic quantum dot”. In: *Physical Review Letters* 110.12 (2013), p. 126803.

[34] Gabriel Alvarez. “Coupling-constant behavior of the resonances of the cubic anharmonic oscillator”. In: *Physical Review A* 37.11 (1988).

[35] Joachim Ankerhold. “Quantum tunneling in complex systems: the semiclassical approach”. In: vol. 224. Springer, 2007, pp. 7–11.

[36] Robert Yaris, John Bendler, and Ronald A. Lovett. “Resonance calculations for arbitrary potentials”. In: *Physical Review A* 18.5 (1978).

[37] Ulrich Weiss. “Quantum Dissipative Systems”. In: vol. 10. WORLD SCIENTIFIC, Oct. 1999, pp. 178–184. ISBN: 978-981-281-787-7. DOI: 10.1142/4239.

[38] Joachim Ankerhold. “Quantum tunneling in complex systems: the semiclassical approach”. In: vol. 224. Springer, 2007, pp. 24–26.

[39] M Kataoka et al. “Tunable nonadiabatic excitation in a single-electron quantum dot”. In: *Physical Review Letters* 106.12 (2011), p. 126801.

[40] Hansjörg Scherer and Benedetta Camarota. “Quantum metrology triangle experiments: a status review”. In: *Measurement Science and Technology* 23.12 (2012), p. 124010.

[41] R. B. Laughlin. “Quantized motion of three two-dimensional electrons in a strong magnetic field”. In: *Physical Review B* 27.6 (1983), p. 3383.